Comparisons of experimental measurements and two-dimensional plasma-fluid numerical simulations of a magnetized plasma column

G. S. Chiu[a] and S. A. Cohen
Princeton University, Plasma Physics Laboratory, P.O. Box 451, Princeton, New Jersey 08543

(Received 1 April 1996; accepted 9 August 1996)

The density, the electron, ion, and neutral temperatures in dense ($n_e > 10^{13}$ cm^{-3}) and cool ($T_e < 8$ eV) magnetized helium plasma columns submerged in a cool neutral gas ($n_0 \sim 3\times10^{15}$ cm^{-3}) environment have been measured. These plasmas, of similar collisionality to those expected in the scrape-off layer of ITER (International Thermonuclear Experimental Reactor) [R. Parker, Contrib. Plasma Phys. **34**, 422 (1994)], are found to obey the low-recycling behavior of approximate plasma pressure balance along the column axis. Density decreases by a factor of about 2 and T_e remains isothermal. Computer simulations using the B2 [R. Schneider *et al.*, J. Nucl. Mater. **196–198**, 810 (1992)] plasma-fluid code have been performed and are in good agreement with experimental results. Measured ion temperatures are consistent with classical energy transfer from the electrons. Neutrals within the plasma are heated by elastic and charge-exchange collisions. This set of measurements represents the most detailed comparisons between experimental results and B2 predictions. © *1996 American Institute of Physics*. [S1070-664X(96)03511-2]

I. INTRODUCTION

The study of plasma behavior near a material boundary has had a long history extending back to Langmuir.[1] Many variables serve to influence the dynamics of such a system, including the mechanics of plasma generation through the breakdown of neutral gas, the interaction of charged plasma particles among themselves and sometimes with neutral gas (for a partially ionized plasma), the introduction of magnetic fields, the material and geometry of the boundary, etc. The applications are equally diverse, among which are plasma processing (etching, ion implantation), probe theory and plasma phenomena near limiters and divertors of tokamaks. Although much is known, many areas still need to be explored and clarified. For example, among earlier theories on dc positive columns,[2] ions are usually assumed cold ($T_i = 0$) or in equilibrium with electrons ($T_i = T_e$), and subsequent plasma properties evaluated on these two bases. On the other hand, ion temperatures are sometimes measured (e.g., near tokamak edge[3]), but their interactions with other species (electrons or neutrals) are often not evaluated. In the realm of plasma modeling through fluid or kinetic codes, detailed T_e, T_i, and sometimes T_n profiles in the scrape-off region of tokamaks can be calculated, but experimental verifications and code validations are often minimal or nonexistent. Efforts to rectify this situation are underway.[4]

The goals of this paper are to present:

(1) Detailed two-dimensional experimental measurements of T_e, T_i, and T_n, among other variables, of plasma columns submerged in a neutral gas environment of sufficient density that interactions are important but not dominant,[5] and
(2) simulations of the above-mentioned phenomena with a broadly used plasma fluid code, with the aim of code testing and validation in a regime of relevance to fusion research.

The paper is organized as follows: Sec. II describes the experimental apparatus. Section III presents the diagnostic system in detail, noting in particular the regimes of application in which these diagnostics are valid. Experimental results and analytical models are given in Sec. IV. The B2 fluid code and simulation results will be discussed in Sec. V.

II. APPARATUS

Helium plasma is produced by a lower-hybrid-waves-heated source[6] in a linear machine, a schematic of which is shown in Fig. 1. Helium is chosen as the working gas to remove the complexity associated with molecular reactions. The source consists of a coaxial cylindrical inconel waveguide, 2.2 cm in diameter and 14.6 cm in length, immersed in an axial magnetic field. Typically, about 700 W of microwave power (2.45 GHz) is fed into a center copper–nickel electrode, positioned coaxially at one end of the waveguide and is electrically isolated from it by an alumina insulator. The waveguide is thus closed at one end but open at the other to allow the outflowing of plasma.

The entire assembly is housed within a stainless steel vacuum chamber, maintained at a base pressure of $<10^{-6}$ Torr. During experiments however, a slow steady-state gas flow is maintained at a constant predetermined pressure P_n. Plasma discharges are typically of 260 ms in duration, and reach quasi-steady-state, characterized by stationary density and temperature profiles, approximately 60 ms after the initial gas breakdown.

The plasma which emerges out of the waveguide flows toward a biasable graphite or copper endplate, typically 7–25 cm away from the waveguide exit. The axial magnetic field serves to confine the plasma into a cylindrical column and enable the propagation and absorption of lower hybrid waves. A magnetic field of 3.5 kG is generated at the center of the chamber via coils arranged in a Helmholtz-coil con-

[a]Present address: University of British Columbia, Department of Physics, Vancouver, V6T 1Z1, Canada.

 1070-664X/96/3(11)/4250/18/$10.00

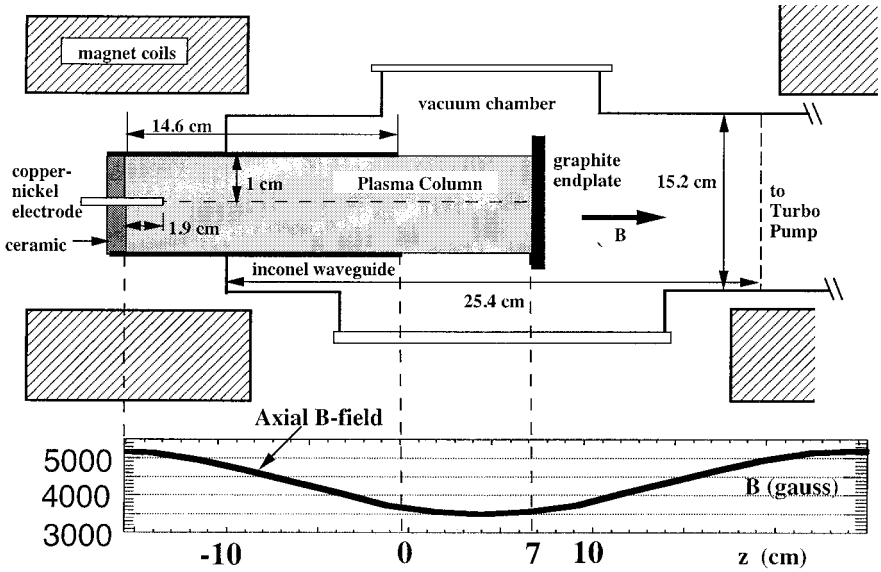

FIG. 1. A schematic of the system configuration, showing the plasma column and end target plate. The nominal magnetic field intensity on axis is also plotted as a function of axial distance.

figuration. A plot of the axial magnetic field is also shown in Fig. 1. Unless otherwise stated, a graphite endplate is positioned to intercept the axial magnetic field perpendicularly in the experiments reported here. Finally, the plasma column is bathed in and allowed to interact with surrounding helium neutral gas, at an operating pressure P_n of up to 100 mT, and monitored by a baratron.

III. DIAGNOSTICS

The plasma has been diagnosed with a single scanning Langmuir probe and a Fabry–Perot interferometer. Furthermore, thermal fluxes have been measured using a thermocouple attached to the target endplate. Each of these diagnostics will be described next.

A. Langmuir probe

The Langmuir probe is constructed of a cylindrical 1-mm-diam tungsten wire, and protrudes 1.02 mm out of a ceramic insulator sleeve. The probe is held stationary throughout each discharge. Typically, 10–15 complete scans of probe I-V data per discharge are collected and stored on a PC. These I-V plots are then deconvolved and averaged to yield a single point in the density (n)—electron temperature (T_e)—plasma potential (ϕ_s) parameter space. Data reproducibility among the scans is good, and uncertainties in the measured n and T_e are typically $\pm 15\%$. The probe is then mechanically translated axially or radially with subsequent plasma discharges. A spatial profile is thus assembled.

Using standard theory,[7] each of the current-voltage (I-V) characteristics is fitted by a least-squares nonlinear fitting procedure to give n and T_e using

$$I(V)=I_{\rm sat}^{+}-I_{\rm sat}^{-}\exp\left(\frac{V-\phi_s}{k_B T_e}\right), \tag{1}$$

where $I_{\rm sat}^{+}$ is the ion saturation current,

$$I_{\rm sat}^{+}=0.5nec_sA_i \tag{2}$$

with the numerical factor 0.5 due to density decrease in the presheath, c_s is the sound speed, and A_i the probe area as presented to the ions. The electron saturation current, or the free Maxwellian electron flux, $I_{\rm sat}^{-}$, is

$$I_{\rm sat}^{-}=0.25ne\left(\frac{8kT_e}{m_e\pi}\right)^{0.5}A_e, \tag{3}$$

with A_e the probe area as presented to the electrons.

The use of Eq. (1) requires several conditions to be satisfied. These include the sheath be thin, the plasma be collisionless near the probe, and magnetic field effects be accounted for. We will now consider each of these effects.

1. Thin sheath approximation

When the sheath dimension is greater or of the order of the probe radius (i.e., $r_p \leqslant \lambda_{\rm D}$, where $\lambda_{\rm D}$ is the Debye length), detailed kinematic and geometric relationships between the interception of particle orbits and the probe surface must be known. This is the orbit-limited regime,[8,9] and generally extends to low-pressure plasmas. On the other hand, if $r_p \gg \lambda_{\rm D} \approx 4\times 10^{-4}$ cm in our case, the probe resembles a flat surface with respect to incoming particle fluxes, and the much simplified thin sheath or planar probe approximation can be employed.[10]

2. Collisional effect

When the probe dimension r_p exceeds collisional mean-free-paths $\lambda_{\rm col}$ (for either electron–ion, electron–neutral, or ion–neutral collisions), the current to the probe is determined by macroscopic transport equations (characterized by particle diffusivity and mobility), and individual single particle motion can be neglected. Generally speaking, collisions impede the free flow of particles to the probe and can cause momentum loss (in unlike collisions). Therefore the current drawn is correspondingly reduced (roughly by the ratio $\lambda_{\rm col}/r_p$[8,9]). In our plasmas, nominally all of the relevant collisional mean-

free-paths ($\lambda_{ei} \sim \lambda_{ee} \sim \lambda_{en,\text{elastic}} \sim 2$ cm and $\lambda_{in} \sim 0.6$ cm) are long compared to r_p, therefore collisional effects are not important.

3. Magnetic field effects

The addition of a magnetic field constrains particles to gyrate circularly around field lines in orbits of radii equal to the Larmor radii ρ_L. Hence cross-field transport is curtailed and particle orbits impinging onto the probe surface are modified, with electrons more greatly affected than ions due to their smaller gyroradii. Accordingly, when ρ_L is much smaller than the probe dimension r_p, as is often the case with electrons, the probe is in the ''magnetized'' regime. Electron flow is then essentially one dimensional, and the effective collection area of the probe as presented to the electrons (A_e) is modified to be the projected cross-sectional area of the probe as intercepted by magnetic field lines. Conversely ions are relatively unaffected if $\rho_{L,i} \geqslant r_p$, and the Bohm current and dynamics are unchanged with respect to previous probe analysis.

In a one-dimensional quasicollisionless theory (when collisional mean-free-path>presheath scale) in strong magnetic fields, it has been shown[10] that ion current is essentially indistinguishable in form from that of the field-free case, provided the ion collection area (A_i) is taken to be the projection of the probe surface in the direction of the magnetic field. Hence we will use the relatively straightforward Bohm formula [Eq. (2)] in our analysis, with the probe area suitably modified for ions and electrons.

Experimentally, in the presence of a magnetic field, it has been observed that the I-V characteristic starts to deviate from the simple exponential relation for voltages above the floating potential V_{fl}, and that the electron to ion saturation current ratio is drastically reduced.[11] In particular, the electron current is found to increase more slowly above the floating potential, an effect attributed to the depletion of electrons along a flux tube into which electrons in the vicinity cannot freely diffuse because of the constraint of a magnetic field.[12] Thus, Tagle *et al.*[13] have shown that the fitted electron temperature will become artificially and increasingly higher than the real value as more data points above the floating potential are included in the fitting procedure. In practice some points need to be included to obtain good statistical fitting in the region near the floating potential. We have adopted the iterative procedure whereby only those data within one T_e above V_{fl} are used in the fitting, resulting in an overestimate in the derived T_e of no more than 20%.[13] Figure 2 shows a typical resultant fit of I-V data to Eq. (1) at $T_e = 3.8$ eV.

Plasma potential ϕ_s is calculated according to[7]

$$\frac{e(V_{\text{fl}} - \phi_s)}{T_e} = 0.5 \ln\left[\left(2\pi \frac{m_e}{m_i}\right)\left(1 + \frac{T_i}{T_e}\right)\right] + 0.5, \qquad (4)$$

where the last term incorporates the presheath drop. We have neglected secondary electron emission, but have estimated that the error is less than 10% in ϕ_s.[14]

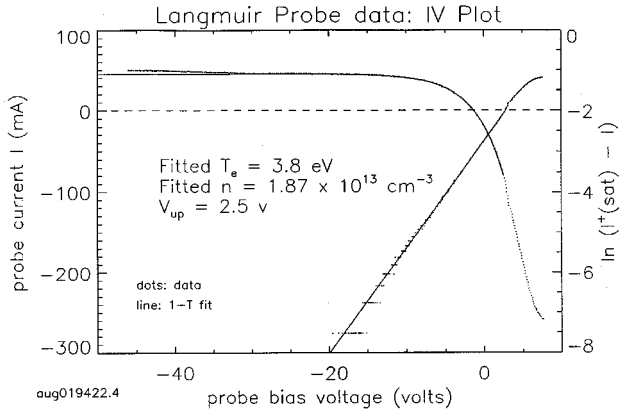

FIG. 2. Typical fit of I-V data of the Langmuir probe.

B. Fabry–Perot interferometer

The determination of ion and neutral temperatures T_i, T_n is performed with a Fabry–Perot (FP) interferometric system, a schematic of which is sketched in Fig. 3. Line-integrated emission from the plasma perpendicular to the magnetic field is wavelength dispersed by a 0.5 m monochromator and then fed into an ''air-plate'' FP interferometer.[15] A central spot (zeroth-order) configuration has been set up. The distance d between the FP plates can be varied by the insertion/substitution of different spacers. In the experiments, a spacer of $d = 0.87 \pm 0.002$ cm is chosen, giving a free spectral range (FSR$\equiv \lambda^2/2d$) of 1.45 Å for the He I line at 5016 Å, and 1.26 Å for the He II line at 4686 Å.

Different portions of the plasma column can be scanned through the use of an adjustable prism which can be axially or radially translated to yield a line-integrated axial or radial profile of the emission. The achieved axial and radial spatial resolutions are 0.1 and 0.25 cm, respectively. Instrumental broadening has been measured (with Ba lines at around 5000 Å and well-fitted by a Gaussian profile) to have a full width at half-maximum $\Delta\lambda_I$ of 0.035 Å.

To filter out the $\sigma_{\pm}$ components of the Zeeman-split lines, a polarized filter is inserted in front of the monochro-

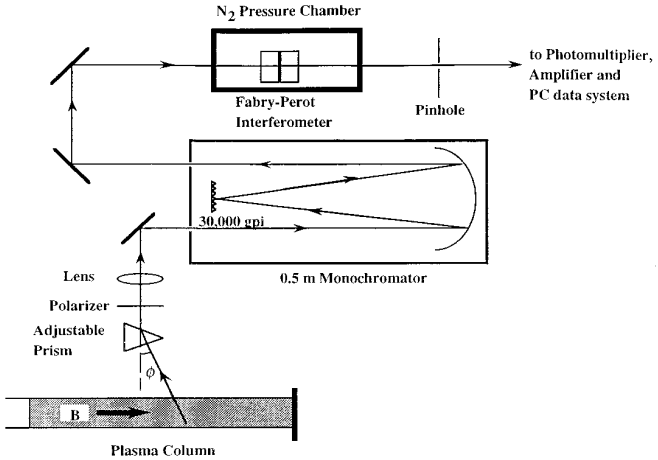

FIG. 3. Schematic of the Fabry–Perot interometric setup used to measure T_i and T_n.

TABLE I. Dipole line transitions used in T_i and T_n measurements. Relative intensities are from Ref. 16.

Species	Wavelength (Å)	Transition	Relative intensities
He I	4713.138	$4s\ ^3S-2p\ ^3P_2$	5.05
	4713.155	$4s\ ^3S-2p\ ^3P_1$	3
	4713.374	$4s\ ^3S-2p\ ^3P_0$	1.02
He I	5015.7	$3p\ ^1P-2s\ ^1S$	1
He I	5875.603	$3d\ ^3D_1-2p\ ^3P_2$	1.2
	5875.618	$3d\ ^3D_2-2p\ ^3P_2$	18
	5875.620	$3d\ ^3D_3-2p\ ^3P_2$	100
	5875.629	$3d\ ^3D_1-2p\ ^3P_1$	18
	5875.644	$3d\ ^3D_2-2p\ ^3P_1$	54
	5875.970	$3d\ ^3D_1-2p\ ^3P_0$	24
He II	4686	4–3, consisting of:	
	4685.979	$4p\ ^2P_{1/2}-3d\ ^2D_{3/2}$	0.63
		$4s\ ^2S_{1/2}-3p\ ^2P_{3/2}$	2.2
		$4p\ ^2P_{3/2}-3d\ ^2D_{5/2}$	1.14
	4685.876	$4f\ ^2F_{5/2}-3d\ ^2D_{5/2}$	5.1
	4685.849	$4f\ ^2F_{7/2}-3d\ ^2D_{5/2}$	100
	4685.802	$4d\ ^2D_{3/2}-3p\ ^2P_{3/2}$	4.2
		$4p\ ^2P_{3/2}-3d\ ^2D_{3/2}$	0.12
	4685.749	$4d\ ^2D_{5/2}-3p\ ^2P_{3/2}$	38.3
		$4f\ ^2F_{5/2}-3d\ ^2D_{3/2}$	70.1
	4685.616	$4p\ ^2P_{1/2}-3s\ ^2S_{1/2}$	5.6
	4685.570	$4s\ ^2S_{1/2}-3p\ ^2P_{1/2}$	1.1
	4685.453	$4p\ ^2P_{3/2}-3s\ ^2S_{1/2}$	11.1
	4685.422	$4d\ ^2D_{3/2}-3s\ ^2S_{1/2}$	21.3

mator in parallel with the applied B-field so that only the π components are selected. Nevertheless, as the upper and lower levels of spectral lines may still be associated with different Lande factors, some influence of the Zeeman splitting remains. This has been taken into account during the data analysis whenever necessary.

Three line transitions (4713, 5016, and 5876 Å) due to He I and the 4686 Å line due to He II have been used to determine the respective neutral and ion temperatures. Their fine structures and relative intensities are tabulated in Table I.[16]

Typically, the measured FP line profiles are fitted by a summation of Gaussian line shapes due to fine structure, and assumed to represent the same temperature (except where noted below). The individual Gaussian line shape is a result of convolution between instrumental broadening (assumed Gaussian) and Doppler broadening (also Gaussian). Furthermore, as alluded to earlier, the effects of Zeeman splitting need to be taken into account in view of the *a posteriori* low ion and neutral temperatures and moderate magnetic field. These split components are assumed to have a uniform distribution in the magnetic quantum number M_J, and accorded equal intensities. The fitted Gaussian half-width $\Delta\lambda_{\rm Fit}$ is then deconvoluted to yield the Doppler half-width $\Delta_{\rm D}$ according to

$$\Delta_{\rm D}=[(\Delta\lambda_{\rm Fit})^2-(\Delta\lambda_I)^2]^{0.5} \tag{5}$$

from which the ion or neutral temperatures can be derived:

$$T({\rm eV})=6.7677\times10^8\ \ {\rm m(amu)}\left(\frac{\Delta_{\rm D}}{\lambda_0}\right)^2, \tag{6}$$

where m is the atomic/ionic mass and λ_0 the center wavelength. Errors in the derived T_i and T_n are estimated to be less than 20% and typically $\pm10\%$ due to uncertainties in wavelength dispersion and quality of fitting.

In order to adopt thermal Doppler broadening as the measure of temperatures, other line-broadening mechanisms must be ensured to contribute little, or adequately accounted for. We have ascertained the effects of natural linewidth,[17] pressure broadening,[18,19] macroscopic motion due to finite spatial resolution,[20] and radiative reabsorption or opacity[21] to be small. On the other hand, effects due to Zeeman broadening, instrumental broadening, and fine-structure splitting are significant and are included as discussed above.

In the case of neutrals, it has been observed that the use of a two-temperature fit (i.e., two Gaussians of differing Doppler widths) can provide a better fit. The existence of such ''cold'' and ''hot'' neutrals has previously been observed in many discharges, including magnetized hollow cathode.[22] A hot neutrals population can be expected physically as a consequence of charge-exchange (CX) processes between hot ions and cold neutrals, and will be discussed in more detail in Sec. IV D 4.

C. Other diagnostics

Current and power fluxes impinging onto the endplate are also measured. In particular, bolometric results are obtained using a copper target (0.13-cm-thick, 5.1 cm radius) being connected to a copper–constantan thermocouple at 3.6 cm from the center.

IV. EXPERIMENTAL RESULTS AND DISCUSSIONS

In this section, experimental measurements with helium plasmas in a neutral gas environment (P_n less than 100 mT) and with a normal endplate (magnetic field perpendicular to the plate surface) will be presented. These include results of density and electron temperature obtained from the Langmuir probe, ion and neutral temperatures inferred from FP interferometry, and bolometric measurements of heat fluxes onto target plates. Brief discussions of the results based on zero- and one-dimensional modeling will also be presented. More detailed two-dimensional simulations with B2 will be given in Sec. V D.

A. Langmuir probe: n, T_e, and ϕ_s

Typical profiles of plasma density n, electron temperature T_e, and potential ϕ_s along the central column axis are shown in Figs. 4(a), 4(b), and 4(c), respectively. The ambient neutral pressure P_n is set at 93 mT, with a coupled input power $\mathcal{P}_e$ (assumed to the electrons only) of 700 W$\pm10\%$. The axial magnetic field at the center of the chamber is 3500 G. Three cases of biases on the endplate at -10, -30, and -50 V are shown, as are typical error bars. The length of the plasma column is set to be 22 cm, with one end of the coaxial waveguide at $z=-15$ cm and the endplate at $z=7$ cm ($z=0$ cm denotes the exit of the cylindrical waveguide, see Fig. 1).

In general, density is found to decrease monotonically toward the endplate by a factor of about 2, while T_e remains

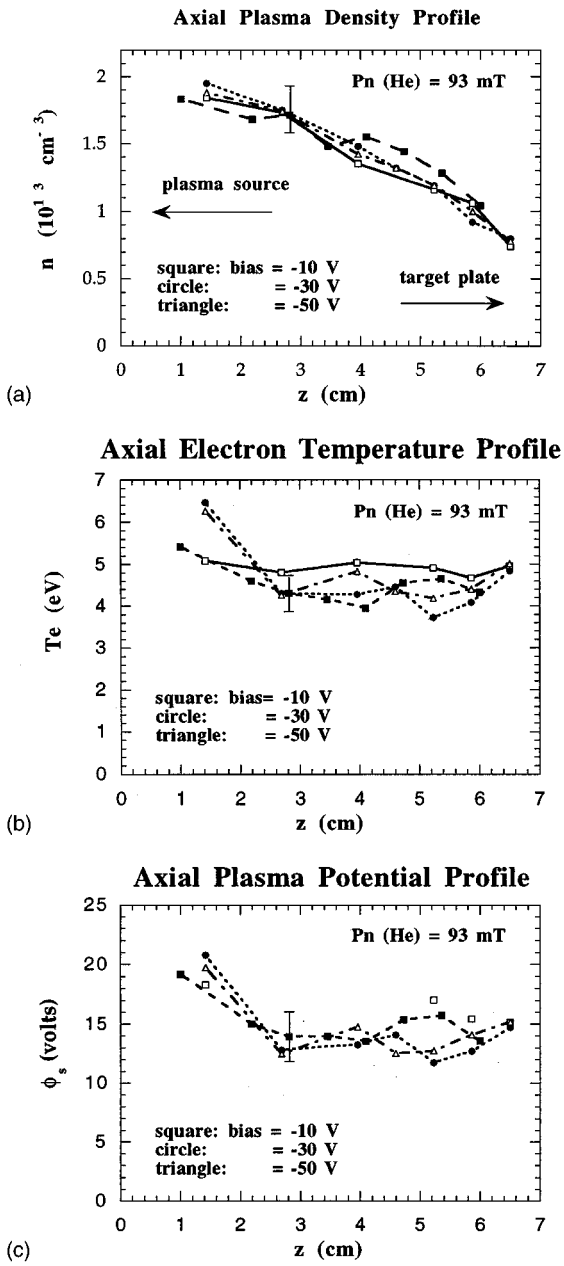

FIG. 4. Axial (a) density, (b) T_e, and (c) potential ϕ_s profiles of helium plasmas at P_n=90 mT under endplate biases of −10, −30, and −50 V.

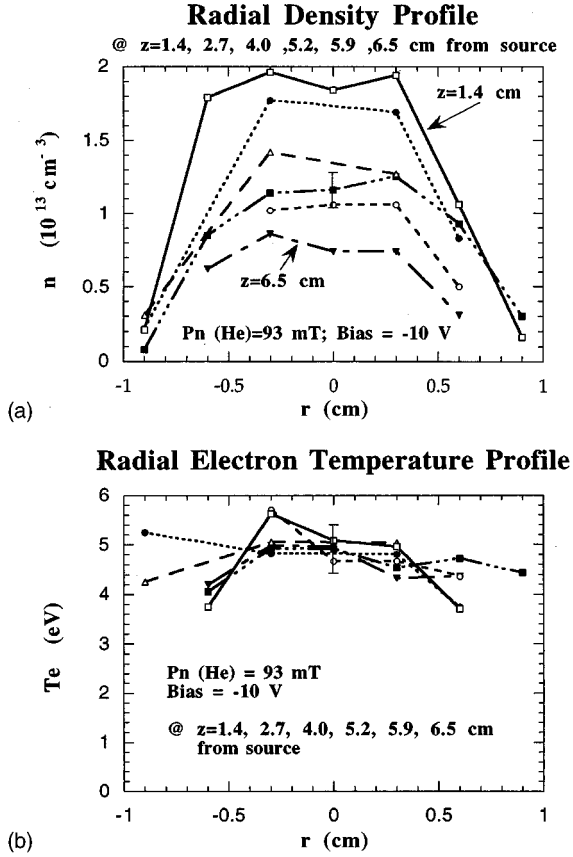

FIG. 5. Radial (a) density and (b) T_e profiles of helium plasmas at P_n=90 mT under endplate biases of −10 V.

approximately isothermal at about 5 eV. Plasma potential has been found to be positive with respect to the chamber walls, as is expected in linear machines where fast axial electron losses are dominant. ϕ_s is also mostly at an equipotential, although there appears to be an initial decrease of $\sim 1 T_e$ (we interchangeably use units of eV or volts for T_e, as required by the context) close to the exit of the waveguide. All three parameters are insensitive to the endplate biases, an indication that the majority of the voltage drop occurs within the sheath, of thickness $\approx 8\lambda_D$ (Ref. 23) $\approx$0.004 cm under present experimental conditions.

Typical radial densities and electron temperatures profiles are shown in Figs. 5(a) and 5(b), respectively. In each, data taken at five different axial positions are profiled. Density exhibits a generally ''flattop'' feature over the central portion, and falls toward zero at the edge, defined approximately by the radius (1 cm) of the inconel cylinder of the waveguide. Density scale lengths remain almost constant (from 0.3 to 0.5 cm) throughout the entire length of the column. The profiles, as a whole, show little diffusive ''flattening,'' indicative of the confining property of the magnetic field and the minor role of radial particle transport compared to axial end losses. T_e, as in the axial case, is nearly isothermal.

The axial variations of n, T_e, and ϕ_s with respect to neutral pressures from P_n=45 to 112 mT are shown in Figs. 6(a), 6(b), and 6(c). We see that density is not sensitive to pressure changes, but T_e (and hence the derived ϕ_s) decreases from ~7 to 4 eV with increasing pressure. This is a well-known consequence of the global balance between generation of plasma ion–electron pairs via impact ionization of neutrals and their losses, and will be discussed in Sec. IV D 1.

Figures 7(a) and 7(b) show the radial dependence of n and T_e on the input power. Three different power inputs are used: a nominal $\mathcal{P}_e$ of 700 W, and two lower levels at 540 and 315 W (both ±10%). At still lower power levels, gas breakdown and discharge generation are not successful. The resultant density and electron temperature profiles for the three cases are shown, all taken at axial position z=0.4 cm from the exit of the plasma cavity. It can be seen that in contrast to the previous variation in ambient neutral pressure, plasma density is now the more sensitive parameter with

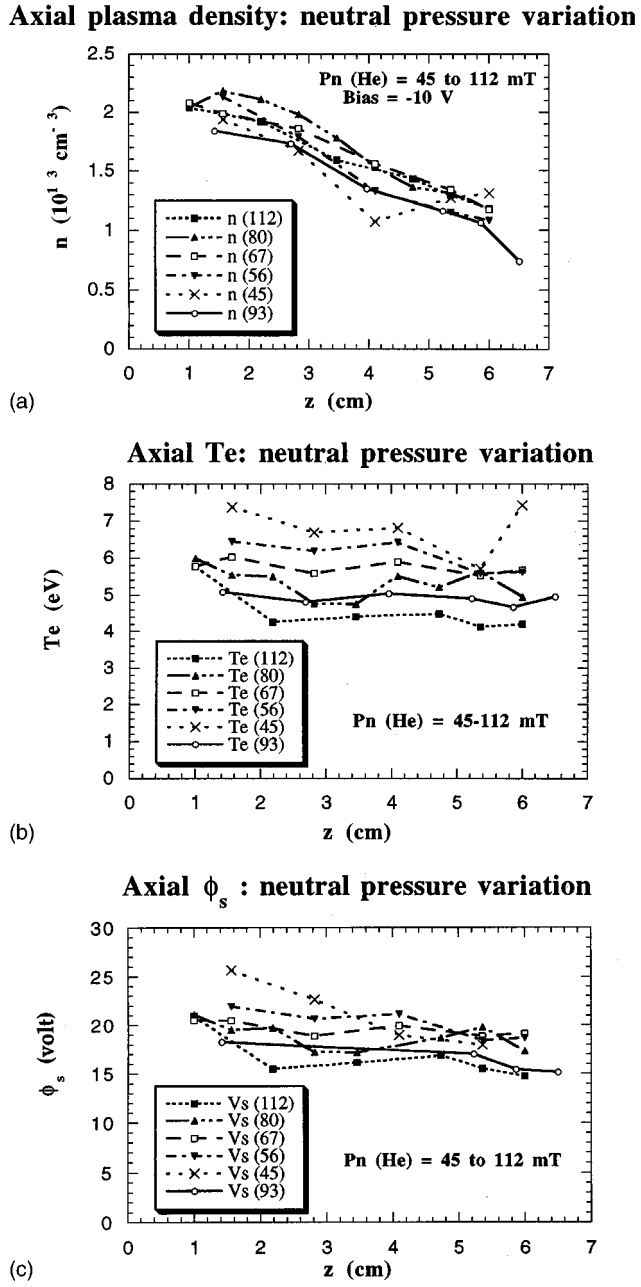

FIG. 6. Axial (a) density, (b) T_e, and (c) ϕ_s profiles with respect to variations in the ambient neutral pressure P_n from 45 to 112 mT. A bias of -10 V is placed on the target plate.

respect to input power, with a decreasing central density with reduced input power. T_e is hardly affected and remains isothermal at ~5 eV.

B. Fabry–Perot interferometer: T_i and T_n

Following the format in Sec. IV A, typical T_i profiles will be shown first, followed by variations with respect to neutral pressure and input power. Next will be measurements of T_n. The distance between the exit of the waveguide and the endplate is fixed at 7.5 cm throughout.

Axial and radial helium ion temperature profiles at neutral pressures varying from 60 to 90 mT are shown in Figs. 8(a) and 8(b). They indicate a close to monotonic decrease

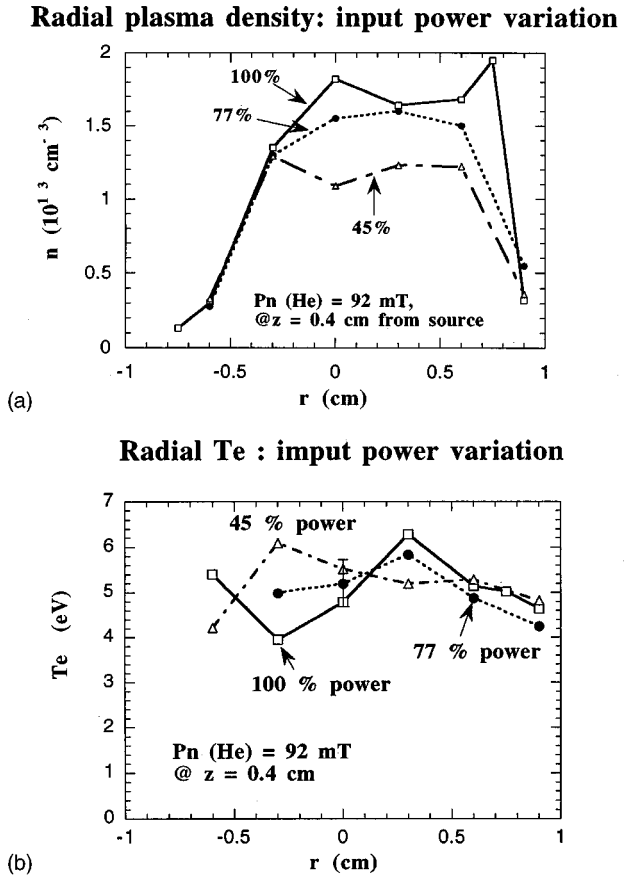

FIG. 7. Comparison of radial (a) n and (b) T_e profile at three different input power levels: 100% (700 W), 77% (540 W), and 45% (315 W) and at $z=0.4$ cm. The ambient neutral pressure is 92 mT.

from ~1 eV near the exit of the waveguide to ~0.5 eV near the endplate. Within experimental uncertainties, the temperatures seem insensitive to the ambient neutral pressures. Radially, it reveals a hotter center and is colder toward the wings. We note that these are line-integrated uninverted temperatures, and that signal-to-noise ratio at the edges becomes increasingly poor, and few points beyond $r=\pm 0.3$ cm are possible. Note that the large density weighing [see Fig. 5(a)] and warmer temperatures at the center would yield only small corrections to the stated line-integrated T_i's were an inversion to local values effected.

The insensitivity of helium T_i with respect to ambient pressure can be noted from Fig. 8(a). In Fig. 9, we have extended the results to a higher pressure at 140 mT. It shows an eventual decrease of T_i at sufficiently high P_n. Our modeling in Sec. IV D 3 indicates that an increasingly collisional plasma (λ_{in} with respect to system length) is the cause.

The axial profiles of T_i with input power are illustrated in Fig. 10. In general, T_i varies directly with the input power. We attribute this to power-dependent density and its role in electron–ion energy collisional transfer, as will be discussed in Sec. IV D 3.

For neutral temperatures T_n, it was found that a two-temperature model (i.e., two Gaussians of differing widths) provided a superior fit to data. Figure 11(a) contrasts the quality of fitting of a one-T fit with that of a two-T fit in Fig.

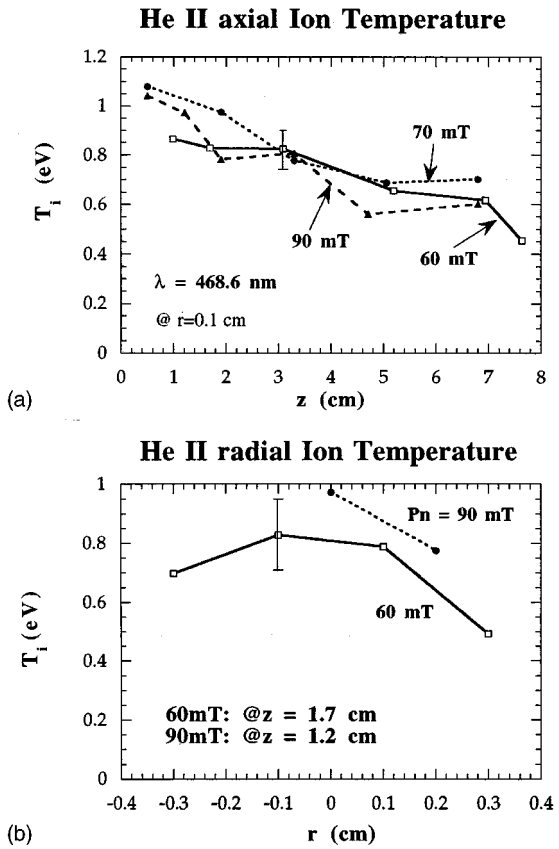

FIG. 8. (a) Axial and (b) radial helium ion temperature profiles from P_n=60–90 mT. The latter is taken at z=1.7 cm when P_n is 60 mT and at z=1.2 cm when P_n is 90 mT.

11(b). For example, the axial T_n profiles using a two-temperature model at 60 mT are presented in Fig. 12. Temperatures derived using He I 4713 Å vs 5016 Å line emission also agree with each other to within experimental uncertainties. There also appears a systematic axial decrease from near the source to the endplate. A hot and cold neutral populations emerge at ~0.5 and 0.1 eV, respectively. In Sec. IV D 4, we attribute these populations to be ambient neutrals penetrating the plasma column from the sideward periphery (as opposed to recycled neutrals emanating from the target plate). The

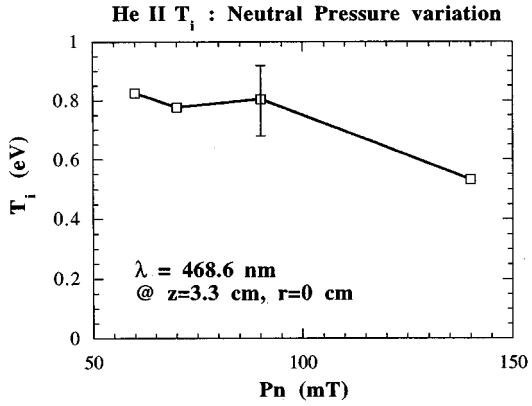

FIG. 9. Helium ion temperature as a function of P_n from 60 to 140 mT.

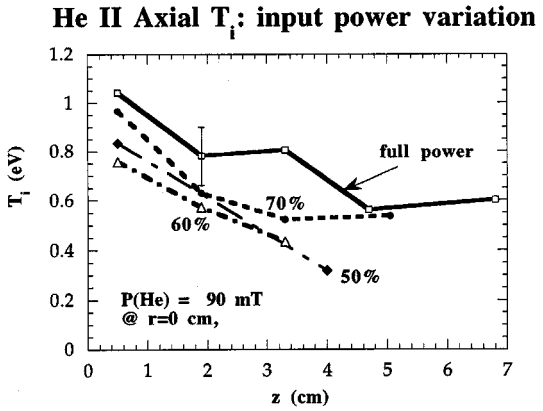

FIG. 10. Ion temperature as a function of input power from 50% to 100% of the nominal input power

cold population is warmed above room temperature due to electron–neutral elastic collisions while the hot population has undergone CX with the ions.

C. Thermocouple: Γ_E

Bolometric measurements of the thermal fluxes impinging onto a floating copper endplate at a variety of neutral pressures have been obtained. The result is shown in Fig. 13. The distance between the exit of the cavity and the endplate

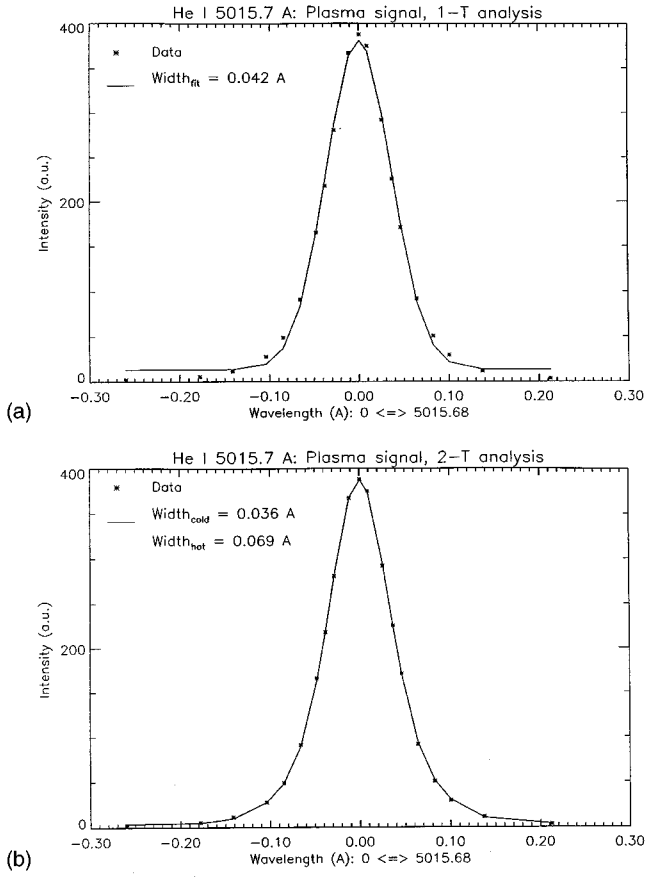

FIG. 11. (a) one-T fit to T_n data; (b) the same set of data is better fitted by a two-T model.

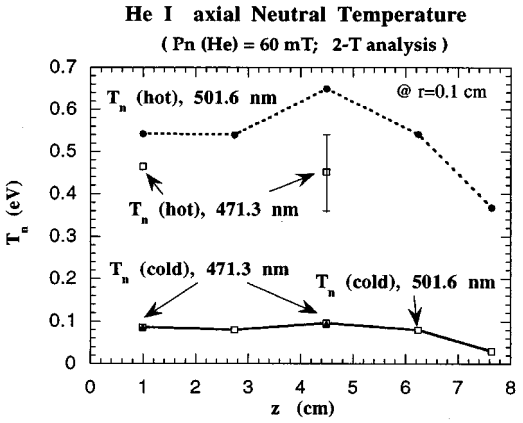

FIG. 12. Axial neutral temperature at P_n of 60 mT. A two-temperature analysis is used.

is set at 10.3 cm here. A constant energy reflection coefficient R_E=0.5 has been assumed for helium ions impinging onto copper.[24]

The results show decreasing power fluxes onto the target with increasing neutral pressures. For biases below the floating potential (see Table II), the measured thermal fluxes also increase as the bias is made more negative. This behavior has been predicted[25] and experimentally verified,[26,27] as the increasing voltage drop brings about greater impact energy of the ions.

D. Discussions

1. T_e vs pressure

To first order, electron temperature can be determined by a particle balance between ion creation against various loss mechanisms such as axial end losses, radial diffusion, or recombination. A simple dependence of T_e on neutral pressure P_n can be derived by equating volumetric ion creation rate via electron impact ionization to an assumed dominant axial loss rate toward both ends of the column. Radial diffusion is deemed unimportant as the strong magnetic field should inhibit transport across magnetic field lines, so that plasma will flow mainly along the magnetic field toward both ends of the column. Such a model was first developed by Tonks and

TABLE II. Floating potential of a cooper endplate at various P_n's.

P_n (mT)	Probe floating potential V_{fl} (V)
60	−10
74	−6.8
90	−3
180	~0

Langmuir[1] for a one-dimensional low-pressure positive column, and was termed the free-fall model as convective sheath-limited flow at sonic speed was purported to be the dominant loss channel. Hence

$$n_0 n_{\rm col} \langle \sigma v \rangle_{\rm ion} \mathscr{V} = 2 n_{\rm sh} c_s \mathscr{A}, \tag{7}$$

where n_0 is the neutral density, $\langle \sigma v \rangle_{\rm ion}$ the ionization rate coefficient, $\mathscr{V}$ the plasma volume, and $\mathscr{A}$ the axial end cross-sectional area. As a first approximation, we take the volume-averaged column density $n_{\rm col}$ ($\approx n_\infty$=density far away from the sheath) to be twice that of the area-averaged density entering the sheath $n_{\rm sh}$.

Noting the temperature dependence using the analytic electron ionization rate coefficient of Seaton[28]

$$\langle \sigma v \rangle_{\rm ion} = C T_e^{0.5} \exp\left(- \frac{\chi_{\rm ion}}{T_e} \right), \tag{8}$$

where $\chi_{\rm ion}$ is the ionization potential and C the constant of proportionality, and that $c_s \propto \sqrt{T_e}$ (assuming small T_i/T_e), Eq. (7) reduces to

$$P_n \propto \exp\left(\frac{\chi_{\rm ion}}{T_e} \right). \tag{9}$$

Thus T_e is predicted to increase inversely as ln P_n decreases, as observed in experiments.

More quantitatively, we have fitted the ionization rate coefficient data for helium[29] with the Seaton formula [Eq. (8)], yielding $C = 7.8 \times 10^{-9}$ cm^3/(s $\sqrt{\rm eV}$). Accordingly, T_e can be calculated analytically by combining Eqs. (7) and (8), viz.

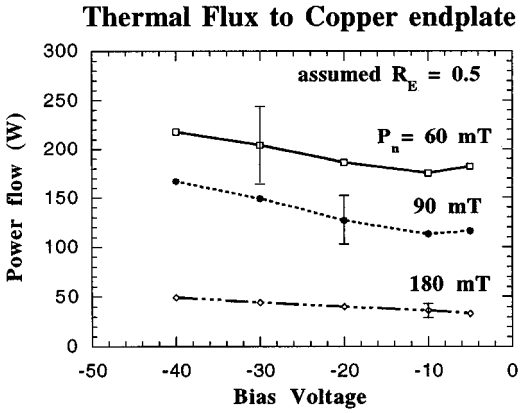

FIG. 13. Thermocouple measurements of thermal fluxes onto a copper endplate at plate biases from −40 to 5 V at three different P_n's.

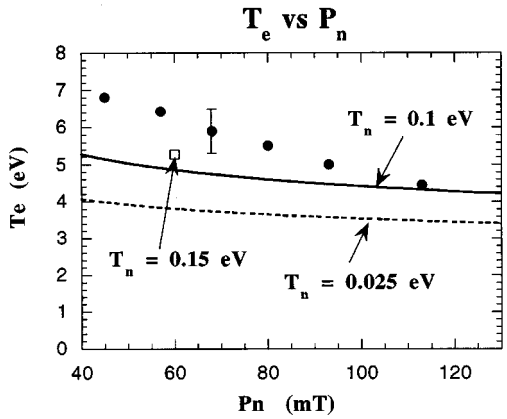

FIG. 14. Comparison between the predicted T_e using Eq. (10) as a function of neutral pressure and experimental measurements.

$$\exp\left(\frac{\chi_{\text{ion}}}{T_e}\right)=\left[1.3\times10^{-2}\left(\frac{L[\text{cm}]}{2}\right)\times\left(\frac{\mu_i[\text{amu}]}{1+T_i/T_e}\right)^{0.5}\frac{1}{T_n[\text{eV}]}\right]P_n[\text{mT}], \quad (10)$$

where the column length L is obtained as $\mathscr{V}/\mathscr{A}$. Taking $L=20$ cm, $T_n=0.1$ eV, the predicted T_e's are shown in Fig. 14, along with experimental values. We remark that a uniform P_n has been assumed (i.e., P_n at column axis$=P_n$ at the periphery as measured by the baratron).

It can be seen that the experimental T_e has a steeper rate of decrease with increasing P_n than the predicted one. This is partly due to the assumption of a constant average neutral temperature. A rising T_n with decreasing P_n as found experimentally (average T_n of 0.1 eV at 90 mT and 0.15 eV at 60 mT) can bring about closer agreement. This is also shown in Fig. 14. The inverse dependence of T_n with P_n is due partly to a drop in T_e and partly to an increase in neutral–neutral collisions (Sec. IV D 4). In summary, it is shown that the observed inverse dependence of electron temperature with neutral pressure is consistent with particle balance in a plasma column flowing predominantly in an axial direction.

2. n vs input power

Considering next energy balance and the variation of plasma parameters with respect to input power, we can follow Motley *et al.*[30] and pose a zero-dimensional power balance between microwave power input to the electrons and various loss channels. At equilibrium, the fraction of input power $\mathscr{P}_e$ (characterized by an efficiency factor η_e) coupled to the electrons is expended as internal energy losses due to ionization and excitation (hence losses through subsequent radiation), as axial convective losses to the ends of the column, and as energy transfer to the ions by collisions. Accordingly,

$$\eta_e\mathscr{P}_e=n_0n_{\text{col}}\langle\sigma v\rangle_{\text{ion}}\chi_{\text{ion}}\mathscr{V}+n_0n_{\text{col}}\times\sum_j(\langle\sigma v\rangle_{\text{ext},j}\Delta E_{\text{ext},j})\mathscr{V}+2n_{\text{sh}}c_s\delta_eT_e\mathscr{A}+n_{\text{col}}\nu_E^{i/e}(T_e-T_i)\mathscr{V}, \quad (11)$$

where $\Delta E_{\text{ext},j}$ is the excitation energy of the jth reaction, δ_e the electron sheath energy transmission factor, and $\nu_E^{i/e}$ the energy equilibration frequency between electrons and ions. It can be seen that given a fixed neutral density (and hence a constant electron temperature from discussions above), Eq. (11) is linear in plasma density, assuming a constant power coupling efficiency η_e.

To test this assertion, we have adopted a simple measure of a ''volume-integrated'' density $\langle n\rangle$ at $z=0.4$ cm for three levels of power input, where

$$\langle n\rangle=\int_{-a}^{a}n(r)rdr\approx\sum_j\frac{n_j+n_{j+1}}{2}\frac{r_j+r_{j+1}}{2}(r_{j+1}-r_j), \quad (12)$$

where r_j is the radial coordinate of the jth data point. The result is shown in Fig. 15. It can be seen that density increases with applied power, although our method has been highly approximate. Motley *et al.*[30] have previously observed an increasing heating efficiency with decreasing input power ranging from 0.5 to 3.5 kW in low-pressure argon plasmas. Our observations are consistent with their results.

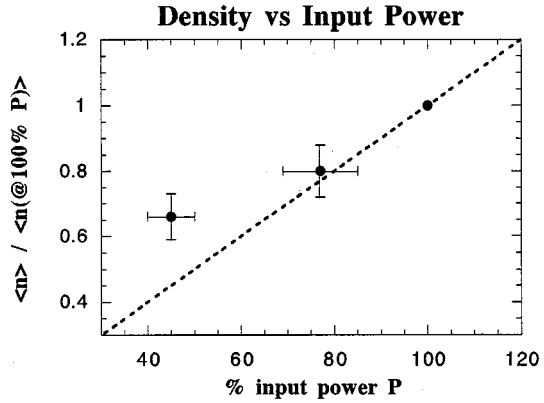

FIG. 15. Measured plasma density as a function of percentage of full input power $\mathscr{P}_e$—100% power denotes 700 W. Density has been normalized by that density obtained with full power.

The relative importance of each loss mechanism can also be assessed. Using previously quoted plasma parameters and system dimensions, ionization losses consume 200 W. Excitation loss rate is comparable at 200 W. With $\delta_e=5.7$ (see Sec. V C), axial end losses are found to be 95 W, while collisional transfer rate to the ions are negligible at 10 W ($\nu_E^{i/e}$ is evaluated in Sec. IV D 3). A total of 505 W is accounted for, compared to a nominal power input of 700 W. The outstanding portion of the power may then be due to radial losses, resistive losses in the cables/electrode, direct ion heating, or less than 100% in heating efficiency η_e. Nevertheless, this simple estimate can be seen to be adequate in describing the overall power balance of our plasma column.

Finally, we note that electron temperature is found to be relatively insensitive to variation in input power. This relatively narrow range of T_e's may be set by physical upper and lower bounds. The upper bound to T_e is set by $\chi_\parallel$, the along-field thermal conductivity. The lower bound to T_e is satisfied by the requirement to generate plasma.

3. Ion temperature T_i

We can gain a heuristic estimate of the ion temperature given the previous results in density and electron temperature. By invoking a zero-dimensional model and assuming classical ion heating via Coulomb collisions with electrons but neglecting CX,

$$\frac{dT_i}{dt}=\nu_E^{i/e}(T_e-T_i), \quad (13)$$

where $\nu_E^{i/e}$ is the electron–ion energy equilibration frequency. The solution, assuming ions are cold initially and electrons isothermal, is

$$T_i=T_e[1-\exp(-\nu_E^{i/e}\tau_i)], \quad (14)$$

where τ_i is the average ion energy loss time between those collisions (either with electrons or neutrals) whereby T_i's are altered. τ_i can be approximated in two ways. First, we as-

sume nearly convective flow and neglect charge exchange. τ_i can be taken to be $L_t/(0.2c_s)$, where L_t (=10 cm) is the tube length and c_s the ion acoustic speed. A slower flow than sonic speed ($0.2c_s$) has been assumed as ion flow is just being initiated inside the waveguide, and represents the average velocity inside the waveguide according to B2 simulations. With helium plasmas at $n_e=3\times10^{13}$ cm^{-3}, $T_e=5$ eV, and using $\ln\Lambda_{ie}=10$, $\nu_E^{i/e}=2.2\times10^4$ s^{-1} and using T_i of 1 eV in c_s, $\tau_i=9.1\times10^{-6}$ s. The resultant ion temperature nearest to the waveguide is 0.9 eV using Eq. (14), a result in good agreement with experimental findings. Note that the amount of ionic cooling due to CX inside the waveguide is expected to be small because of the lower neutral density.

However, CX collisions with ambient cold neutrals are expected to lead to substantial ion cooling outside the waveguide. Hence we estimate T_i when ions are heated by electrons in between CX as follows: τ_i is approximated by $\lambda_{CX}/\bar{v}$, where λ_{CX} is the mean-free-path for charge exchange, and $\bar{v}$ is the average ion flow velocity in between CX collisions whereupon ions are cooled. This formulation has assumed an ion retaining no ''memory'' of its former state after each CX event, and adopting the colder neutral temperature and thus would be reheated again. With the same plasma parameters as above, λ_{CX} is 0.65 cm (Ref. 29) assuming a neutral density of 7.5×10^{14} cm^{-3} (i.e., $P_n=90$ mT, $T_n=0.1$ eV). Again, assuming a slower plasma flow to be at 20% of the sound speed as a CX event would also dissipate ion momenta, the expected T_i [from Eq. (14)] is found to be 0.35 eV, also in fair agreement with experimental values.

Thus we have shown that classical electron–ion heat exchange, moderated by charge exchange outside the waveguide, is sufficient to account for the observed ion temperatures. However, this simple analysis has neglected ion thermal conduction process as another possible cooling mechanism as well as direct ion heating due to nonlinear wave absorption and other plasma instabilities or turbulences. Lower hybrid waves have been predicted[31] and observed[32] to mode convert and be absorbed by ions.

The dependence of ion temperature on ambient neutral pressure and input power can also be understood within this model. That T_i decreases as neutral pressure P_n increases (more so downstream near the target plate than near the waveguide/source) is a consequence of increasing ion–neutral (charge-exchange) collision rate and a shortened τ_i. T_i decreases as axial distances increases due to more numerous collisions with neutrals as ions flow toward the endplate.

As plasma density decreases with decreasing input power, so T_i should also decrease as power is lowered as there are fewer energy equilibration collisions with electrons between the comparatively constant charge-exchange collisions. Indeed, as $\langle\sigma v\rangle_{CX}$ stays roughly constant at low energies, the relative mean-free-path $\lambda_{CX}\propto v_{th,i}$ (ion thermal velocity) is seen to decrease for a lower T_i, inviting even more frequent collisions with neutrals.

By viewing the line emission across the applied magnetic field (Fig. 3), we have, strictly speaking, been measuring the perpendicular ion temperature $T_{i,\perp}$, as opposed to the parallel (along-field) temperature $T_{i,\parallel}$. The distinction can be of great importance in plasma processing, where anisotropic velocity distributions are usually desired for etching purposes. Under our experimental conditions, the ion cyclotron frequency for helium at $B=3.5$ kG is $f_i=1.3\times10^6$ s^{-1}, whereas the ion–neutral collision frequency is $\nu_{CX}=9.8\times10^5$ s^{-1} while $\tau_i^{-1}=10^4$ s^{-1}. Therefore, ions are only weakly magnetized and are confined long enough so that collisions are sufficient to ensure $T_{i,\perp}\sim T_{i,\parallel}$.

4. Neutral temperature T_n

Turning now to an estimate of the neutral temperature T_n, we will again utilize an analytical model accounting for neutral heating by collisional transfer from electrons (elastic scattering) and ions (charge exchange), and cooling via equilibration through collisions with a background of colder neutrals. Hence,

$$\frac{dT_n}{dt}=\nu_{en}\left(\frac{2m_e}{m_n}(T_e-T_n)\right)+\nu_{CX}(T_i-T_n)\,\delta(t-t_{CX})-\nu_{nn}\left(\frac{T_n-T_{bg}}{2}\right), \tag{15}$$

where $\nu_{en,CX,nn}$ are the collision frequencies for electron–neutral elastic scattering, charge–exchange, and neutral–neutral collisions, respectively, and $T_{bg}=0.025$ eV is the cold neutral background temperature. The $\frac{1}{2}$ in the last term is to indicate an average energy loss by the hotter particle of half of the energy difference in a neutral–neutral collision. Ion–neutral elastic scatterings are neglected since they parallel CX processes and are peaked in the forward direction.[33] We have also included the delta functions $\delta(t-t_{CX})$ in the charge–exchange term to signify the fact that this event is a discontinuous process. Thus the neutral acquires a ''hotter'' temperature immediately after a charge–exchange event that would take place at most once (at time $t=t_{CX}$ during the residence time τ_{res} of the neutral in the plasma). This *ansatz* follows from the expected length scale ordering $\lambda_{CX}\gg r$ (characteristic plasma length scale=radius of plasma column=1 cm)$>\lambda_{nn}$, λ_{en}, and will be checked for consistency later.

The solution to Eq. (15) is

$$T_n(t=\tau_{res})=\frac{\mathscr{A}}{\mathscr{B}}\left[1-\left(1-\frac{\mathscr{B}T_0}{\mathscr{A}}\right)\exp(-\mathscr{B}\tau_{res})\right], \tag{16}$$

where

$$\mathscr{A}=\nu_{en}\frac{2m_e}{m_n}T_e+\nu_{nn}\frac{T_{bg}}{2},$$

$$\mathscr{B}=\nu_{en}\frac{2m_e}{m_n}+\frac{\nu_{nn}}{2},$$

and $T_0\equiv T_n(t=0)$ is the initial neutral temperature.

The neutral residence time τ_{res} will be evaluated as follows: assuming the radial movement across the plasma column is diffusive in character, then

$$\tau_{res}\approx\left(\frac{r}{\lambda_{eff}}\right)^2\tau_{eff}, \tag{17}$$

where λ_{eff},τ_{eff} are the effective collision mean-free-path and effective collision time, respectively, given by

$$\lambda_{\text{eff}}^{-1}=\lambda_{\text{CX}}^{-1}+\lambda_{nn}^{-1},$$
$$\tau_{\text{eff}}^{-1}\equiv\nu_{\text{eff}}=\nu_{\text{CX}}+\nu_{nn}, \tag{18}$$

as both the momentum-altering processes of charge-exchange and neutral–neutral collisions govern the diffusive movement of a neutral particle (hence electron–neutral elastic scattering is neglected as little momentum is imparted to the neutral particle).

Using experimental values of $T_e=5$ eV, $T_i=1$ eV, plasma density $n_e=n_i=3\times10^{13}$ cm^{-3}, and neutral density $n_0=3\times10^{15}$ cm^{-3} (at 90 mT and T_n of 0.025 eV) would yield the following (the first value for an assumed cold neutral of $T_n=T_{\text{bg}}$ and second value for a hot neutral of $T_n=T_i$): $\lambda_{en}=0.05$–0.33 cm,[34] $\lambda_{\text{CX}}=2.0$–9.8 cm, and $\lambda_{nn}=0.16$–1.0 cm.[35] The neutral residence time is therefore $\tau_{\text{res}}=290-5.5$ μs. We note that the previous ansatz in length scale ordering is satisfied. Consequently, with an initial T_0 of 0.025 eV (no charge exchange has taken place), a cold neutral is warmed to 0.05 eV, whereas a hot neutral ($T_0=T_i=1$ eV, denoting an initial charge exchange event at $t_{\text{CX}}=0$) will be cooled to 0.66 eV. Charge exchange taking place between $t=0$ and $t=\tau_{\text{res}}$ will result in neutral temperatures intermediate between the two values above. This range is in good agreement with that observed experimentally as well.

In conclusion, we have found that cold neutrals are slightly heated (i.e., to higher than room temperature) due to electron–neutral energy transfer while hot neutrals, a consequence of charge exchange with ions, are expected to retain a higher temperature within the radial dimension of the plasma column.

V. B2 SIMULATION RESULTS AND DISCUSSIONS

B2 (Ref. 36) is a two-dimensional multifluid code designed to simulate edge and scrape-off-layer plasmas in tokamaks and has been used extensively in the fusion community.[37] It is originally set up for toroidally symmetric configurations, but has been modified to our cylindrical geometry. In the code, a reduced set of fluid equations, namely particle continuity, momentum, and energy equations are solved and plasma properties such as density, flow velocity, and temperatures are computed. Other quantities such as particle or thermal fluxes can then be evaluated.

The description of plasma states using a fluid code dictates that gradient scale lengths should be larger than particle collisional mean-free-paths. A two-dimensional kinetic treatment has yet to be achieved, hence fluid simulation results are often the only available tools. Fortunately, early studies on low-pressure, dc positive columns[2] have demonstrated that it is possible to apply fluid equations over a wide range of neutral pressures.

The presence of a strong magnetic field constrains charged particle motion to principally the parallel direction. Thus, the requirement on mean-free-paths is usually of relevance in the axial direction only. A quick estimate of the collisionality found in our helium plasmas with $n=2\times10^{13}$ cm^{-3} and $T_e=5$ eV reveals the electron–electron mean-free-path $\lambda_{ee}\equiv v_{\text{th},e}/\nu_{ee}$ to be 1.8 cm. Assuming a typical axial plasma scale length $L_\parallel$ (dimension, gradient length, etc.) of 10 cm, plasma collisionality $\nu^*\equiv L_\parallel/\lambda_{ee}$ is about 6. In the case of ions with $T_i=1$ eV, the corresponding ion–ion mean-free-path is $\lambda_{ii}=0.1$ cm. The fluid approximation is found to be valid for both electrons and ions nominally, but will be questionable near the plasma column edge where densities are lower.

In B2, transport parallel to the magnetic field, as well as friction and energy equilibration, obeys classical theory. Cross-field transport is assumed to be anomalous with specified transport coefficients. Quasineutrality is assumed, while plasma–neutral interactions are treated by means of neutral source/sink terms. Currently, neither CX, ion–neutral elastic, nor neutral–neutral collisions are treated in B2. Furthermore, the plasma is assumed to be current free (ambipolar flow only), and the presheath electric field which plays a role in the acceleration of ions, is not solved for explicitly; rather, an end point flow speed (e.g., sonic flow) is imposed at the boundary. Cross-field drift terms are not included.

Although B2 has been used extensively in the fusion community as an analytical and predictive tool for the edge region, scant attention has been paid experimentally to corroborate its predictions in detail, primarily because of difficult access and diagnosis of tokamaks. One of the goals of our experiments is to utilize and cross-check B2 with the detailed experimental results obtained so far. Accordingly, we have used B2 to simulate the experimental plasma column and its interaction with ambient neutrals surrounding it.

Section V B below is a detailed description effected in B2 to adapt to our particular experimental conditions. Section V C briefly discusses the imposed boundary conditions, while Sec. V D presents simulation results.

A. Equations of B2

B2 assumes all species to be sufficiently collisional to behave as fluids, and seeks to solve the first three moments of the Boltzmann equation, i.e., continuity, parallel momentum, and ion and electron energy balance following the formulation of Braginskii.[38] A two-dimensional description, both along-B-field (x) and cross-field (y) direction, is used. Assuming that the helium plasma consists of electrons and singly charged ions (hence $n_i=n_e\equiv n$), five equations governing the evolution of density n, the parallel and radial fluid velocity u and v, the electron and ion temperatures $T_{e,i}$ are derived. At steady-state, B2 finds simultaneous solutions to the following nonlinear coupled system:

(i) Continuity equation:
$$\frac{\partial(nu)}{\partial x}+\frac{\partial(nv)}{\partial y}=S_n. \tag{19}$$

(ii) Ion momentum balance in the x direction:
$$\frac{\partial}{\partial x}\left(mnu^2-\eta_x\frac{\partial u}{\partial x}\right)+\frac{\partial}{\partial y}\left(mnvu-\eta_y\frac{\partial u}{\partial y}\right)=-\frac{\partial(P_i+P_e)}{\partial x}+S_{mu}. \tag{20}$$

(iii) Anomalous diffusion in the y direction:
$$v=-\frac{D_\perp}{n}\frac{\partial n}{\partial y}. \tag{21}$$

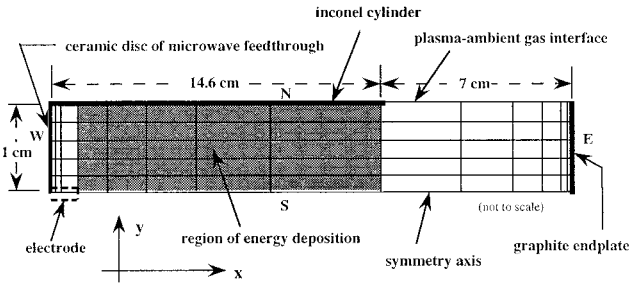

FIG. 16. The computational mesh used in B2 simulations in order to model an azimuthally symmetric cylindrical geometry. The ''N(north),'' ''S(south),'' ''W(west),'' and ''E(east)'' designations are explained in the text. The shaded area denotes the region of microwave power deposition. See also Fig. 1 for comparison.

(iv) Electron energy balance:

$$\frac{\partial}{\partial x}\left(\frac{5}{2}nuT_e - n\kappa_x^e\frac{\partial T_e}{\partial x}\right)+\frac{\partial}{\partial y}\left(\frac{5}{2}nvT_e - n\kappa_y^e\frac{\partial T_e}{\partial y}\right)$$

$$= u\frac{\partial P_e}{\partial x} - k_{ei}(T_e - T_i) + S_E^e. \tag{22}$$

(v) Ion energy balance:

$$\frac{\partial}{\partial x}\left(\frac{5}{2}nuT_i + \frac{1}{2}mnu^3 - \kappa_x^i\frac{\partial T_i}{\partial x} + \frac{1}{2}\eta_x\frac{\partial u^2}{\partial x}\right)+\frac{\partial}{\partial y}\left(\frac{5}{2}nvT_i + \frac{1}{2}mnvu^2 - \kappa_y^i\frac{\partial T_i}{\partial y} + \frac{1}{2}\eta_y\frac{\partial u^2}{\partial y}\right)$$

$$= -u\frac{\partial P_e}{\partial x} + k_{ei}(T_e - T_i) + S_E^i \tag{23}$$

where m=mass of the ion, $P_{e,i}$=electron and ion pressure=$nT_{e,i}$, $\eta_{x,y}$=parallel and radial viscosity coefficient, $D_\perp$=traverse particle diffusion coefficient, $\kappa_{x,y}$=parallel and radial thermal conduction coefficient, k_{ei}=electron–ion energy equilibration coefficient, S_n, S_{mu}, $S_E^{e,i}$=volumetric sources of particle, momentum, and electron or ion energy, associated with various plasma–neutral interactions, recombination, and radiation

B. Code description

1. Geometry

We have assumed azimuthal symmetry in cylindrical geometry to conform to the two-dimensional requirement of B2. The computational region is nominally 21.6 cm axially by 1.0 cm radially. A rectangular grid is devised, where the x and y coordinates denote the parallel and radial direction, respectively.

A schematic diagram of the computational domain is illustrated in Fig. 16. The bottom (''south'') boundary represents the symmetry axis of the plasma column. The first 14.6 cm of the top (''north'') boundary corresponds to the surface of the enclosing inconel waveguide (the microwave feedthrough), while the remaining 7 cm is treated as open boundary where ambient neutrals can interact with the plasma. The left (''west'') boundary corresponds to the closed end surface of the inconel cylinder, while the right (''east'') boundary represents the plasma–sheath interface, which, due to the extreme narrowness of the sheath, is practically coincident with the graphite endplate.

2. Power deposition profile

An *ad hoc* profile is used for the microwave power deposition profile. Such an approach has previously been employed by Porteous and Graves,[39] where a cylindrical magnetically confined low-pressure argon positive column is modeled.

The total input power (assumed exclusively) to the electrons $\mathscr{P}_e$ is specified. Inside the waveguide (inconel cylinder), the power deposition spatial profile is assumed to be uniform along the x direction but follows the radial profile:

$$P(x,y) = P_0\frac{e^b - e^{b(y/a)}}{e^b - 1}, \tag{24}$$

where P_0 is the power density so that $\mathscr{P}_e$ would be recovered when $P(x,y)$ is integrated over the region of power deposition, and a the radius of the column. No power is deposited outside the waveguide, as no rf wave has been detected.[6] This particular profile is chosen as it is capable of mimicking a wide variety of radial heating profiles depending on the flatness factor b [from almost ''flat'' (large positive b) to linear (small b) to ''spiky'' at the center (negative b)], and falling to zero at the edge ($y=a$).

We remark here that though Eq. (24) can assume a variety of shapes through variation in b, resultant simulation results do not exhibit significant sensitivity either in the density or temperature profiles. We have varied b from 0.1 (linear) to 2.0 (''quadratic-like'') to 10.0 (flat), and have found that both axial and radial temperatures vary by less than $\pm 5\%$. Axial and radial densities vary by up to $\pm 20\%$, but still within experimental uncertainties.

3. Neutral particles and atomic physics

a. Recycled neutrals. A prescribed fraction [given by the recycling coefficient $\mathscr{R}=1.0$ (Ref. 24)] of the ion flux impinging onto the target is recycled as neutral particles with a fixed predetermined energy $E_0=3$ eV.[24] The fluxes of these recycled neutrals, as opposed to those of ambient neutrals penetrating from the plasma-neutral periphery, are estimated to be less than 0.2% of the total neutral fluxes. Henceforth these neutrals emanating from the target plate are divided into a number of angular rays, the flux intensity of which is determined by a chosen distribution $F(\theta)$ [e.g., cosine distribution $F(\theta)=\cos\theta$ where θ is the angle between the plate normal and the ray]. Each of these rays is tracked as it traverses across the plasma, undergoes electron-impact ionization/excitation, until it is completely exhausted or passes out of the plasma volume. This ray treatment is justified if λ_{ion} is long compared to the dimension of the column.

b. Ambient neutrals. In a closed geometry at high power flow, the recycling of neutrals serves as a primary fueling source for the plasma and strongly influences plasma properties near the target. In our open geometry and lower power flow, where recycling neutrals can pass through the plasma and surrounding neutrals are free to interact with the plasma column, recycling exerts a far less substantial effect.

TABLE III. Excitation energies of singlet and triplet low-lying states ($1s$-nl, $n=2,3$; $l=s,p$) from the ground state ($1s^2$) of helium.

Excited state	Excitation energy (eV)
$2s\ ^1S$	20.614
$2p\ ^1P$	21.217
$3p\ ^1P$	23.086
$2s\ ^3S$	19.818
$2p\ ^3P$	20.963
$3s\ ^3S$	22.717
$3p\ ^3P$	23.006

In its stead, interactions between plasma and ambient neutral particles, especially at high neutral pressures, constitute the more important factor in determining plasma properties and dynamics.

We have assumed a constant neutral density in the plasma column. This is because ionization mean-free-path is long compared to the plasma radius, and the neutral particle is transparent to the plasma. The ambient neutral pressure P_0 thus suffuses throughout the plasma volume. This assumption would not be valid were CX or neutral–neutral collisions included.

c. Electron impact ionization. Ionization provides a source of plasma ions (and electrons). Electron energy suffers a loss equal to the ionization potential $\chi_{\rm ion}(=24.59$ eV in the case of helium atoms in ground state), while ions are assumed to gain the equivalent of the energy of the neutral particle. The collisional-radiative rate coefficients $S_{\rm CR}$, which take into account stepwise ionization, are from Reiter *et al.*[29] The respective particle, momentum, and energy sources/sinks per volume are

$$\begin{aligned} S_n^{\rm ion} &= n_e n_0 S_{\rm CR}, \\ S_{E,e}^{\rm ion} &= -\chi_{\rm ion} S_n^{\rm ion}, \\ S_{E,i}^{\rm ion} &= +T_0 S_n^{\rm ion}. \end{aligned} \tag{25}$$

d. Electron impact excitation. Although inelastic electron–neutral collision does not give rise to a new source of ions, it is often a dominant means of energy loss for electrons as it requires at least 80% of $\chi_{\rm ion}$ to populate each of the excited states. With their respective excitation rate coefficients comparable to that of ionization, it can be seen that collisional excitation represents a substantial expenditure of electron energy. A fully collisional-radiative model is required to account for all such processes, and is beyond the approximation inherent in our present neutral model. Seven states of excitations, namely, those from the ground state ($1s^2$) to $2p\ ^1P$, $3p\ ^1P$, $2s\ ^1S$, $2s\ ^3S$, $2p\ ^3P$, $3s\ ^3S$, and $3p\ ^3P$, are considered, and collectively lead to an electron energy loss of

$$S_{E,e}^{\rm excit} = -n_e n_0 \sum_{j=1}^{7} \langle \sigma v \rangle_{{\rm excit},j} \mathscr{E}_{{\rm excit},j}, \tag{26}$$

where $\mathscr{E}_{{\rm excit},j}$ is the threshold excitation energy for state j, listed in Table III. The rate coefficients are from Janev *et al.*[40]

4. Other parameters

Cross-field transport has been modeled by anomalous but constant radial transport coefficients. The nominal values are: particle diffusion coefficient $D_\perp=1$ m^2/s; transverse ion viscosity $D_\eta=1$ m^2/s, with an ion viscosity coefficient $\eta_y=m_i n D_\eta$; thermal electron and ion conductivities $\chi_e=3$ m^2/s and $\chi_i=1$ m^2/s, with thermal diffusivities $\kappa_y^{e,i}=n\chi_{e,i}$. These values are commonly used to simulate the scrape-off-layer transport properties in tokamaks. We note that for our parameters, the Bohm diffusion coefficient for cross-field transport is ~ 1 m^2/s.

For comparison purposes only, the cross-field diffusion coefficient due to ion–neutral collisions[41] is comparable to $D_\perp$:

$$\begin{aligned} D_{i-n} &= \frac{D_\parallel}{1+(\omega_i\tau_{in})^2} \rightarrow \frac{\rho_i^2}{\tau_{\rm CX}} \\ &\text{when } (\omega_i\tau_{in})^2 \approx (\omega_i\tau_{\rm CX})^2 \gg 1, \end{aligned} \tag{27}$$

where ω_i is the ion gyrofrequency, ρ_i the ion Larmor radius, and $D_\parallel \sim (\lambda_{\rm CX})^2/\tau_{\rm CX}$ the along-field diffusion coefficient. With $P_n=90$ mT, $T_n=0.1$ eV, and $T_i=0.5$ eV, $(\omega_i\tau_{\rm CX})^2=5.3$ and D_{i-n} is found to be 2.5 m^2/s.

C. Boundary conditions

A boundary condition is required for each of the fluid equations in Sec. V A: continuity, momentum, electron, and ion energy. At both ends in the axial (x) direction, a sheath (sonic flow) condition is imposed to simulate a floating target plate. Constant ion and electron energy transmission factors are assumed, which can take into account the sheath potential drop. Energy transmission factors $\delta_{i,e}$ are defined in the form:

$$\begin{aligned} Q_i &= \delta_i T_i \Gamma, \\ Q_e &= \delta_e T_e \Gamma, \end{aligned} \tag{28}$$

where $Q_{i,e}$ are the energy fluxes carried by ions or electrons across the sheath onto the target plates and Γ the particle flux. Following Stangeby[7] and Bissell *et al.*,[42] $\delta_{i,e}$ are given by

$$\begin{aligned} \delta_i &\simeq 2 \\ \delta_e &= \frac{2}{1-\gamma_e} - \frac{1}{2}\ln\left[2\pi\frac{m_e}{m_i}\left(1+\frac{T_i}{T_e}\right)(1-\gamma_e)^{-2}\right], \end{aligned} \tag{29}$$

where γ_e is the secondary electron emission coefficient. For helium plasmas with $T_i \ll T_e$ and neglecting secondary electrons, δ_e is ~ 5.5. An additional presheath potential drop of $\sim 0.7T_e$ is expected to exist in the plasma to accelerate the ions. A secondary electron emission coefficient of 0.15 is used as an average between that of electrons impinging on graphite (the target) and on nickel (the inconel waveguide).[24] Consequently, we have taken the values of $\delta_{i,e}$ to be 2.5 and 5.7 throughout the B2 simulations.

On the south boundary representing the central plasma axis and the symmetry plane, we employ a no-gradient (or no-flux) condition for all the plasma variables, whereas on the north boundary representing approximately the edge of

TABLE IV. Imposed boundary conditions in B2 simulations. $\nabla_{\parallel} \equiv \partial/\partial x$ while $\nabla_{\perp} \equiv \partial/\partial y$. $\Gamma_{n,Ee,Ei}$ are the particle, electron, and ion thermal fluxes, respectively; ''in'' and ''out'' signify the inside and outside of the inconel cylinder.

Variable φ	North in	out	South	West	East
Density	$\nabla_{\perp} n = 0$	Fixed λ_n	$\Gamma_n = 0$	$\nabla_{\parallel} n = 0$	$\nabla_{\parallel} n = 0$
Velocity	$\nabla_{\parallel} u = 0$	$\nabla_{\parallel} u = 0$	$\nabla_{\perp} v = 0$	$u = c_s$	$u = -c_s$
T_e	Fixed T_N	Fixed λ_{Te}	$\Gamma_{Ee} = 0$	$\Gamma_{Ee} = \delta_e T_e \Gamma_n$	$\Gamma_{Ee} = \delta_e T_e \Gamma_n$
T_i	Fixed T_N	Fixed λ_{Ti}	$\Gamma_{Ei} = 0$	$\Gamma_{Ei} = \delta_i T_i \Gamma_n$	$\Gamma_{Ei} = \delta_i T_i \Gamma_n$

the plasma discharge, density and temperature scale lengths are prescribed. Typical values are 0.1 cm for density, and 0.3 cm for temperatures. A no-shear condition for the velocity is also imposed. Table IV summarizes the boundary conditions on the four sides.

D. Results and discussions

1. Standard case for helium

We first investigate B2 simulations with helium plasmas at an ambient neutral pressure $P_n = 90$ mT and an applied power $\mathcal{P}_e = 700$ W. The dimension of the plasma discharge is 21.6 cm in length and 1 cm in radius. Power is assumed to be deposited between the end of the microwave electrode (at $x = 1.9$ cm) and the end of the inconel waveguide (at $x = 14.6$ cm) (see Fig. 16). As only the region beyond the waveguide has been diagnosed, simulation results from $x = 14.6$ cm onwards will be shown, with the axial dimension rescaled to begin at $z = 0$ cm. Hence, plasma will exit the waveguide at $z = 0$ cm, and be terminated by the endplate at $z = 7$ cm. Both electron impact ionization and excitation are included. The additional parameters used consist of a uniform ambient neutral temperature of 0.1 eV throughout the plasma column, and a power deposition flatness factor b [Eq. (24)] of 2. T_n of 0.1 eV is chosen as a gross average of hot charge-exchanged neutrals and the cold background. The above set of parameters shall be referred to as the ''standard-case'' calculation.

Figures 17(a) and 17(b) are the simulation results for axial density, T_e and T_i profiles. Where relevant, experimental data from Sec. IV A have been superimposed for comparison. In addition, the parallel flow velocity, normalized by the local sound speed to yield the local Mach number M, is also plotted. It can be seen that in general (except for T_i near the source), there is excellent, better than $\pm 10\%$, agreement between B2 and experimental results. A low-recycling regime is obtained, characterized by the familiar density decrease of a factor of ~ 2 and an almost isothermal T_e due to a strong electron thermal conductivity. Heat flow is seen to be sheath limited (i.e., convective). The local flow is found to have reached $M \sim 0.5$ upon exiting the waveguide. As a note of interest, M is predicted to be stagnant at $x \sim 8$ cm (i.e., inside the inconel tube), where T_e is also at a maximum.

Ion temperatures are seen to diverge between experimental and calculated values near the plasma source. One plausible reason is due to strong ion heating via charge exchange (CX) by recycled neutrals inside the inconel cylinder. These recycled/reflected neutral particles, typically of energy of ~ 10 eV [assuming an energy reflection coefficient of 0.5 (Ref. 24)] are effectively confined inside the cylinder, and can interact with the ions frequently before escaping. We have estimated the relative heating rate due to CX to that of classical electron–ion equilibration to be

$$\frac{Q_{\mathrm{CX}}}{Q_{ei}} \sim \frac{(T_n - T_i)\,\nu_{\mathrm{CX}}}{(T_e - T_i)\,\nu_{ei}} = 4.6.$$

As this process has not been taken into account in B2, the calculated T_i's are consequently lower than experimental measurements. Once outside the cylinder, such neutrals are quickly lost, ending further ion heating.

The corresponding radial profiles are presented in Figs. 18(a) and 18(b). Density profiles are peaked at the center, and are generally in fair agreement with experiments. Elec-

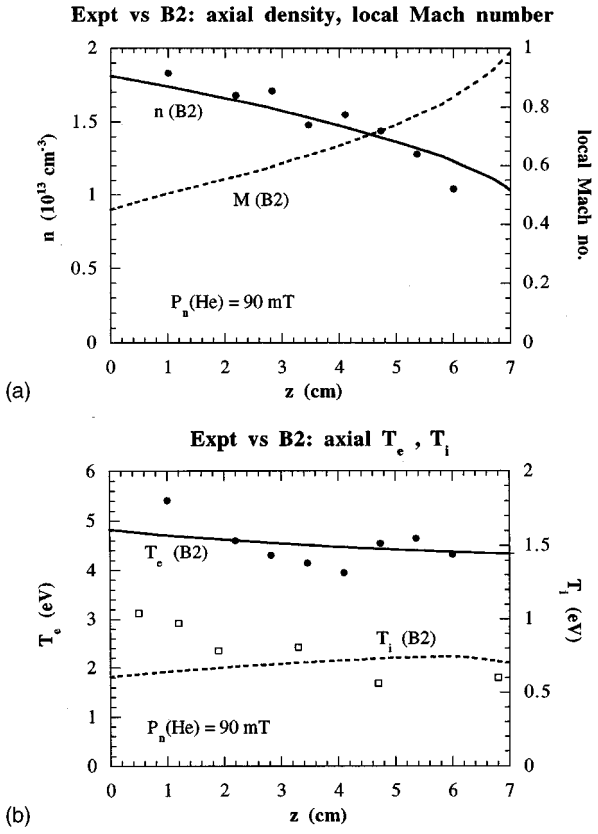

FIG. 17. B2 simulation results of a helium plasma column at 90 mT. The input power to the electrons is set at 700 W, and a flatness factor b of 2 is used. (a) The axial density is shown along with experimental results (dots). The predicted local Mach number is also shown. (b) Axial T_e and T_i profiles from B2 and experiments.

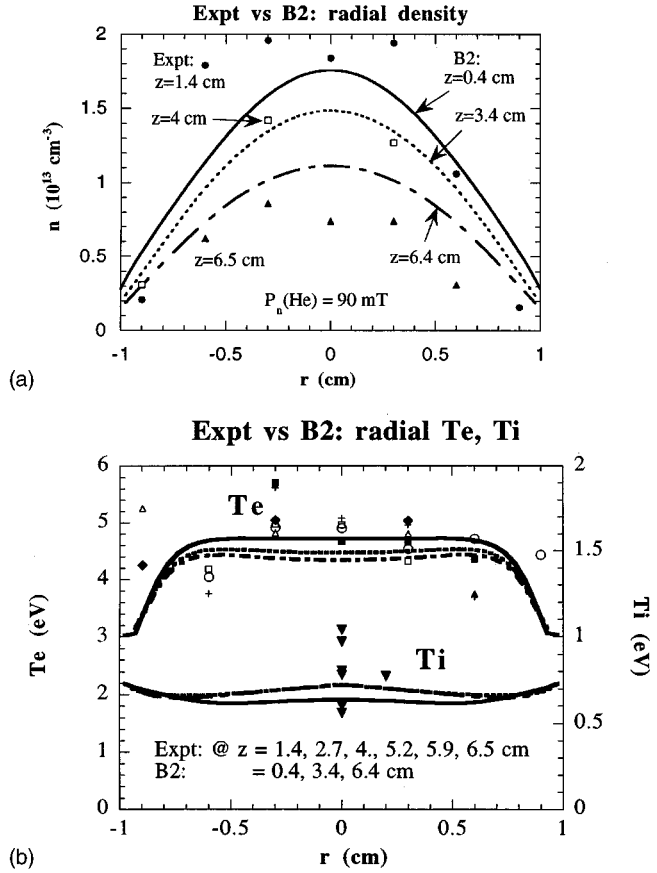

FIG. 18. (a) Measured and B2 results of the radial density profiles at three axial positions. Simulation conditions are as Fig. 16. (b) Measured and B2 results of the radial T_e and T_i profiles.

tron temperature profiles are found to be flat throughout most of the radial extent of the plasma column, also in good agreement with data. Due to the boundary condition of a negative scale length and also the eventual fall-off of the heating profile, T_e is calculated to decrease at the edges. Calculated ion temperatures are also shown to be isothermal. No sensitivity to $D_\parallel$ and $\chi_\parallel$ is shown. We thus can conclude that using realistic input values measured from experiments (P_n, $\mathscr{P}_e$, etc.) and appropriate atomic physics, B2 is able to produce close agreement with experimental spatial profiles in n, T_e, and T_i.

In terms of particle and energy balance, results from B2 have suggested the following, tabulated in Table V. Power end losses are overwhelmingly through electron channels, and are about equally distributed among ionization, excitation (i.e., via radiation), and axial convective end losses. However, the loss channel titled ''ionization'' will reappear as energy of recombination as the plasma impacts the plates. Thus, an additional power of 90 W will be deposited onto the cylinder (west), 73 W to the plate (east), and 39 W lost radially. These results are in fair agreement with our previous zero-dimensional estimate in Sec. IV D 2. In particular, it compares favorably with experimental plate current of 3 A. The calculated heat flux to the plate of [(77+73) W=] 150 W also compares well with measured value of 120 W (see Fig. 13).

Radial losses are found to contribute about 20% in the

TABLE V. Particle and power loss channels in helium plasma according to B2 results. The total input power is ~700 W. Axial losses shown are convective, and more energy will be deposited onto the plates via plasma recombination.

Loss channel	Integrated current flux (A)	Integrated electron energy flux (W)	Integrated ion energy flux (W)
Axial: to cylinder (''west'')	3.7	96	4
Axial: to plate (''east'')	3.0	77	5
Radial	1.5	81	3
Ionization→recombined		202	
Excitation		166	
Total:	8.3	622	15

energy balance. The total power sums to 640 W, which is within the numerical accuracy of the given input of 700 W. It has previously been found that though $\mathscr{P}_e$ is specified, the exact integrated power deposited can vary up to 10% due to grid coarseness.

2. Variations with input parameters

a. Neutral pressure P_n. Figures 19(a) to 19(c) concern the effect of neutral pressure P_n on density and temperatures. Additional simulation runs at neutral pressures of 45, 60, and 110 mT have been made, in approximate accordance with experimental data obtained at 45, 56, and 112 mT. The ambient neutral temperature has been set at 0.1 eV, although previous measurements have revealed a slighter hotter average T_n of 0.15 eV at 60 mT. Hence another run with T_n=0.15 eV has also been performed for comparison. Figure 19(a) shows the results of axial densities, with experimental data offset from B2 results for additional clarity. It may be seen that density is not a sensitive parameter with respect to neutral pressure, as observed in experiments. The trend, however, points to an increase in density with increasing P_n.

T_e is found to vary inversely with P_n, as can be seen from Fig. 19(b). Furthermore, the run made at an ambient neutral temperature of 0.15 eV is found to better describe measurements, thus confirming the sensitivity of not P_n, but the ratio P_n/T_n, or the neutral density n_0, which is the determining factor in overall particle balance, as discussed in Sec. IV D 1. There is seen an increase of ~10% in T_e between the run with T_n=0.15 eV and that with 0.1 eV. Note that although T_e has not proven to be very sensitive to P_n, other quantities such as conductive heat flow ($\propto T_e^{3.5}$) or ionization rate will depend much more critically on P_n.

Finally, ion temperature is also relatively insensitive to the neutral pressure [Fig. 19(c)], as is observed in experiments. Nevertheless, B2 does register a slight decrease in T_i with decreasing P_n, a consequence of higher T_e and therefore a less efficient collisional coupling between ions and electrons during their residence times in the plasma column. Again, the discrepancy near the plasma source is noted.

b. Input power $\mathscr{P}_e$. With regard to the dependence on input power, B2 simulations support experimental findings that density scales directly with power $\mathscr{P}_e$. This is shown in Fig. 20(a), where power fractions of 45%, 77%, and 100% with respect to the standard power input of 700 W have been

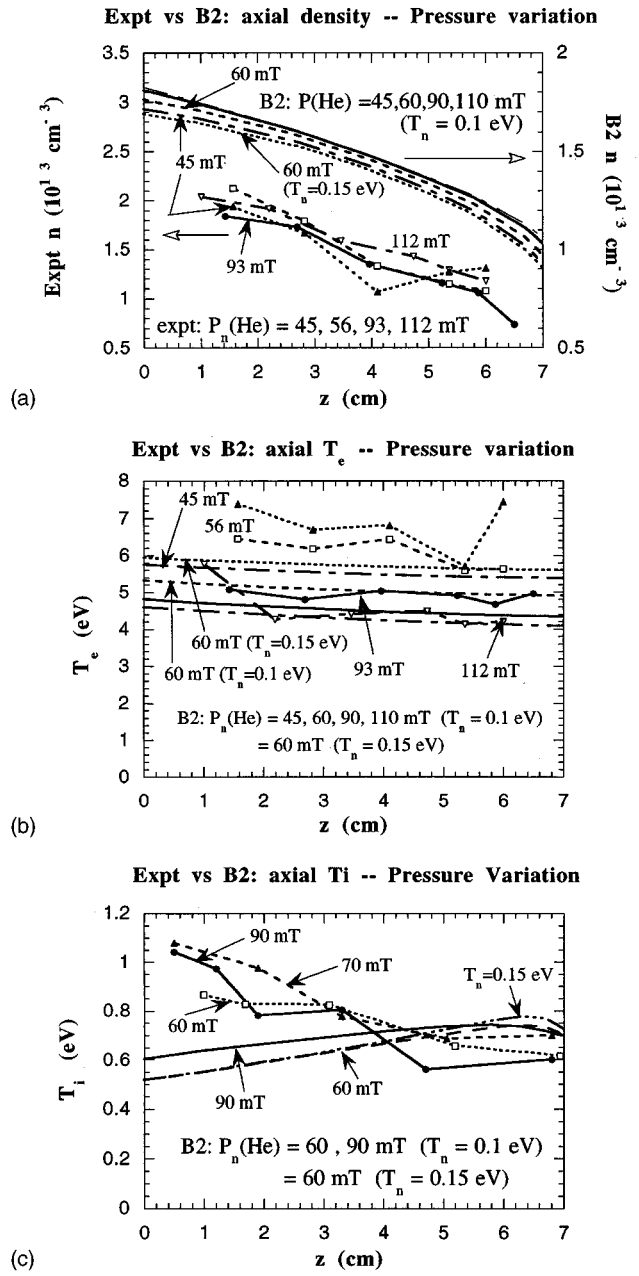

FIG. 19. Experimental and B2 results of the axial (a) density, (b) T_e, and (c) T_i profile as a function of neutral pressures P_n. Note the offsetting of axes between B2 and experimental results in (a).

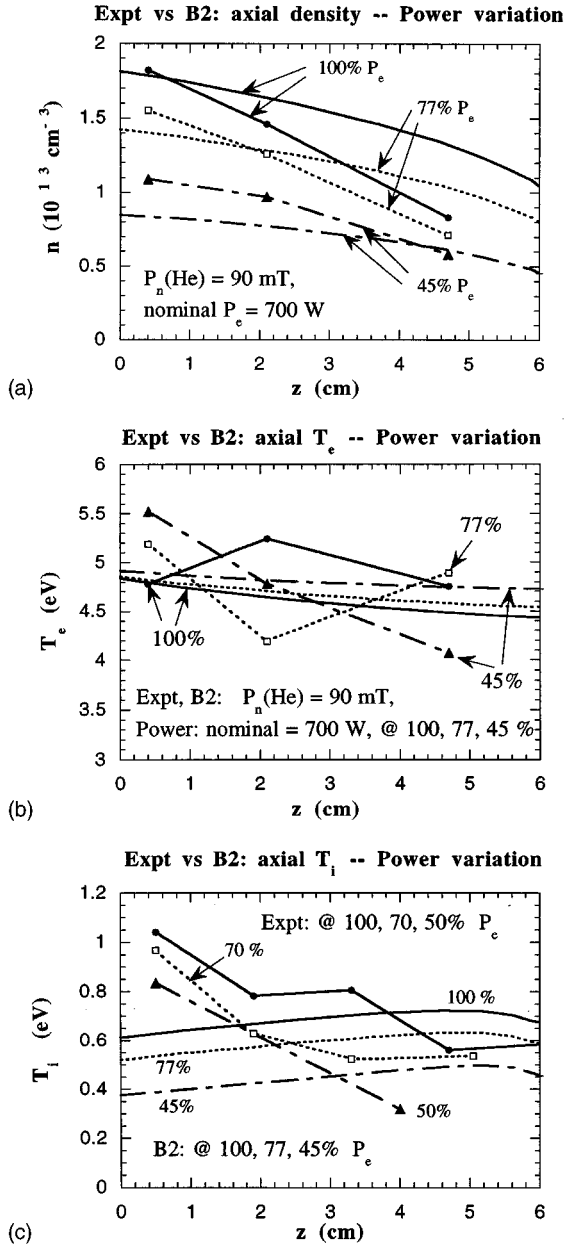

FIG. 20. Experimental and B2 results of the axial (a) density, (b) T_e, and (c) T_i profile as a function of input power $\mathscr{P}_e$.

simulated to compare with experimental measurements. The cylinder exit-plate separation in these B2 results is reset to 6 cm, as is the case in experiments.

The agreement between B2 and data is only qualitative: the calculated rate of axial density decrease is slower than measured. On the other hand, Fig. 20(b) indicates that T_e is not sensitive to the input power, while Fig. 20(c) shows T_i to vary directly with $\mathscr{P}_e$. Both modeling results concur with experimental findings qualitatively.

c. Radial transport coefficients. As cross-field transport coefficients are taken to be anomalous and therefore untested in our experiments, we have proceeded to vary sets of $D_\perp$, χ_e, and χ_i with respect to the standard case. In particular, two additional sets of $(D_\perp, \chi_e, \chi_i) = (0.3,1,0.3)$ and $(2,5,2)$ [m^2/s] have been used. The variations in axial density and temperatures are shown in Figs. 21(a) and 21(b). As expected, a lesser cross-field diffusion limits radial losses, raises central density, and lowers electron temperature by increasing particle confinement time. Central ion temperatures are seen to rise correspondingly due to an increase in ion–electron equilibration frequency.

Overall variations are more sensitive for densities ($\pm 30\%$) and T_i ($+36\%$, -14%) but less so for T_e ($\pm 7\%$). In this connection we note that the use of spatially varying cross-field transport coefficients can lead to closer agreement among measured and simulated values. Axial end losses are also somewhat insensitive ($\pm 15\%$), while radial losses are significantly reduced or enhanced (-64% vs $+51\%$). Radial bolometry should provide the most sensitive test in this aspect.

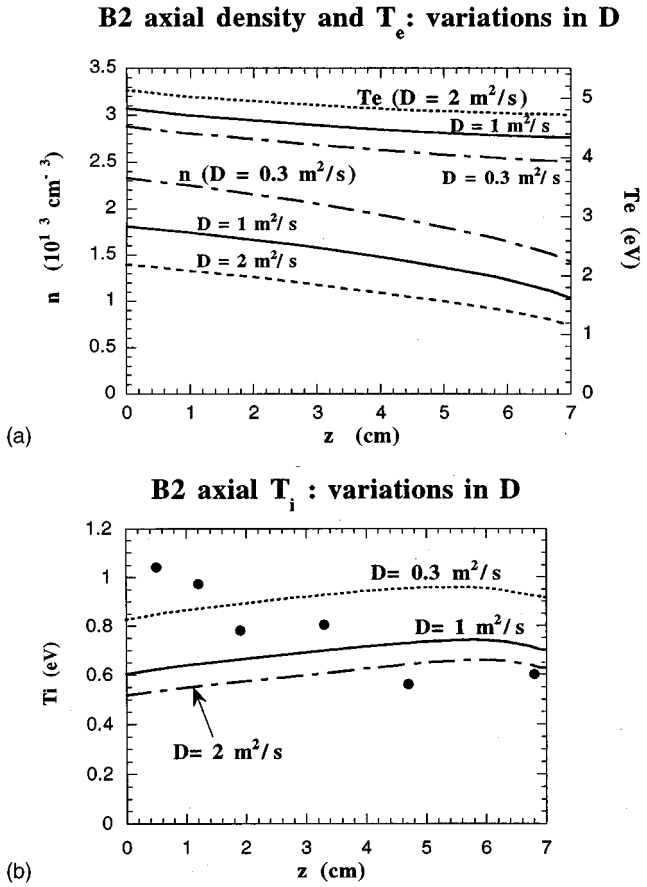

FIG. 21. Sensitivity studies of axial (a) density and T_e, and (b) T_i to radial transport coefficients $D_\perp$, χ_e, and χ_i.

VI. CONCLUSIONS

We have measured n, T_e, T_i, T_n, and ϕ_s of helium plasmas with parameters similar to those expected in the vicinity of divertor plates of magnetic fusion energy (MFE) reactors where substantial amount of neutral gas exists. Variations in ambient neutral pressure and input power have been obtained. For the neutral pressure range within which we have restricted our attention ($P_n<100$ mT), all the results are broadly consistent with theoretical predictions of a one-dimensional collisionless presheath model, moderated by explicit neutral interactions.

In particular, ion and neutral temperatures have been measured in these plasmas. Classical ion–electron equilibration and charge exchange are found to account adequately for the observed T_i, though reflected neutrals are possibly important in some region of the plasma column. Elastic electron–neutral, charge-exchange, and neutral self-collisions are shown to reproduce the measured T_n.

We have also modified and run B2 in order to simulate the experimental conditions. Simulation results generally match very well with experimental measurements in density, electron, and ion temperatures, both axially and radially. Various externally controllable input parameters have been perturbed and their resultant trends have also been reproduced by B2. These data cross-checking have placed confidence in both B2 and our experimental findings. Within the confines of the simple analytical neutral model, we have found that electron-impact ionization and its associated excitation to be determining factors in particle and energy balance.

Nevertheless, the simulation model can be improved by incorporating more detailed neutral dynamics. Recent simulations[43] have ascertained the importance of including neutral–neutral collisions self-consistently when the neutral density is of the order of 10^{14}–10^{15} cm^{-3}. In particular, they have shown significant energy transport through neutral convection in these regimes.

On the other hand, these experimental data can form a basis for testing fluid codes with more advanced neutral models.[4,44] A more complete set of experimental quantities such as plasma flow velocity, spatially resolved neutral densities and pressures, axial and radial heat flow should also complement and enhance code testing and validation.

ACKNOWLEDGMENTS

We extend our thanks to J. Park, T. Bennett, E. Tolnas, and J. Schwarzmann for fine technical assistance.

This work was supported by the U.S. Department of Energy under Contract No. DE-AC02-76-CH0-3073.

[1]L. Tonks and I. Langmuir, Phys. Rev. **34**, 876 (1929).
[2]See for example, S. A. Self and H. N. Ewald, Phys. Fluids **9**, 2486 (1966); H. N. Ewald, F. W. Crawford, and S. A. Self, J. Appl. Phys. **38**, 2753 (1967); D. B. Illc, *ibid.* **44**, 3993 (1973).
[3]G. M. McCracken, S. A. Cohen, H. F. Dylla, C. W. Magee, S. T. Picraux, S. M. Rossnagel, and W. R. Wampler, *Proceedings, 9th EPS Conference Controlled Fusion Plasma Physics*, Culham Laboratory, Abingdon (European Physical Society, Petit-Lancy, 1979), p. 89.
[4]For example, M. E. Fenstermacher, G. D. Porter, M. E. Rensink, T. D. Roglien, S. L. Allen, D. N. Hill, C. J. Lasnier, T. Leonard, and T. Petrie, J. Nucl. Mater. **220–222**, 330 (1995).
[5]See for example, W. Hsu, M. Yamada, and P. Barret, Phys. Rev. Lett. **49**, 1001 (1982); L. Schmitz, R. Lehmer, G. Chevalier, G. Tynan, P. Chia, R. Doerner, and R. W. Conn, J. Nucl. Mater. **176&177**, 522 (1990); G. Fiksel, M. Kishinevsky, and N. Hershkowitz, Phys. Fluids B **2**, 837 (1990); G. S. Chiu and S. A. Cohen, Phys. Rev. Lett. **76**, 1248 (1996).
[6]R. W. Motley, S. Bernabei, and W. M. Hooke, Rev. Sci. Instrum. **50**, 1586 (1979).
[7]P. Stangeby, in *Physics of Plasma-Wall Interaction in Controlled Fusion*, edited by D. Post and R. Behrisch (Plenum, New York, 1986), p. 41.
[8]F. Chen, in *Plasma Diagnostic Techniques*, edited by R. Huddlestone and S. Leonard (Academic, New York, 1965), Chap. 3.
[9]L. Schott, in *Plasma Diagnostics*, edited by W. Lochte-Holtgreven (North-Holland, Amsterdam, 1968), Chap. 11.
[10]I. Hutchinson, *Principles of Plasma Diagnostics* (Cambridge University Press, New York, 1987).
[11]R. Bundy and D. Manos, J. Nucl. Mater. **121**, 41 (1984); K. Guenther, A. Herrmann, M. Laux, P. Pech, and H.-D. Reiner, J. Nucl. Mater. **176 & 177**, 236 (1990).
[12]P. Stangeby, J. Phys. D **15**, 1007 (1982).
[13]J. Tagle, P. Stangeby, and S. Erents, Plasma Phys. Controlled Fusion **29**, 297 (1987).
[14]E. W. Thomas, in Nucl. Fusion suppl.: *Data Compendium for Plasma-Surface Interactions*, 94 (1984).
[15]J. Hirschberg, J. Hesser, E. Hinnov, and N. Rynn, Phys. Fluids **10**, 1114 (1967).
[16]For He I: J. Brochard, J. Phys. Rad. **13**, 433 (1952); W. L. Wiese, M. Smith and B. Glannon, *Atomic Transition Probabilities, Vol. 1: Hydrogen through Neon* (U.S. Bureau of Standards, Washington, DC, 1966), NSRDS-NBS-4; A. Catherinot, B. Dubreuil, and G. Gousset, Phys. Rev. A **21**, 618 (1980). For He II: G. Series, Proc. R. Soc. London Ser. A **226**, 377 (1954)
[17]H. Griem, *Plasma Spectroscopy* (McGraw-Hill, New York, 1964).
[18]H. Griem, *Spectral Line Broadening by Plasmas* (Academic, New York, 1974).

[19]W. L. Wiese and G. A. Martin, in *A Physicist's Desk Reference*, edited by H. L. Anderson (American Institute of Physics, New York, 1989), Chap. 5.
[20]W. L. Wiese, in Ref. 8, Chap. 6.
[21]H. Drawin and F. Emard, Z. Phys. **243**, 326 (1971).
[22]C. Timmermans, A. Lunk, and D. Schram, Contr. Plasma Phys. **21**, 117 (1981)
[23]N. Hershkowitz, in *Plasma Diagnostics Vol. 1: Discharge Parameters and Chemistry*, edited by O. Auciello and D. L. Flamm (Academic, New York, 1989), Chap. 3.
[24]K. Ertl and R. Behrisch, in Ref. 7, p. 515; E. Parilis, L. Kishinevsky, N. Turaev, B. Baklitzky, F. Umarov, V. Verleger, S. Nizhnaya, and I. Bitensky, *Atomic Collisions on Solid Surfaces* (North-Holland, New York, 1993).
[25]P. Stangeby, Phys. Fluids **27**, 682 (1984).
[26]G. V. Roslyakov and G. I Fiksel, Sov. J. Plasma Phys. **12**, 136 (1986); G. Fiksel, Ph.D. thesis, University of Wisconsin—Madison, 1991.
[27]S. Mazusaki, N. Ohno, and S. Takamura, J. Nucl. Mater. **223**, 286 (1995).
[28]M. J. Seaton, Planet. Space Sci. **12**, 55 (1964).
[29]D. Reiter, J. Nucl. Mater. **196–198**, 80 (1992), and references therein.
[30]R. W. Motley, S. Bernabei, W. M. Hooke, and D. L. Jassby, J. Appl. Phys. **46**, 3286 (1975).
[31]M. Brambilla, Plasma Phys. **18**, 669 (1976).
[32]J. J. Schuss, S. Fairfax, B. Kusse, R. R. Parker, M. Porkolab, D. Gwinn, I. Hutchinson, E. S. Marmar, D. Overskei, D. Pappas, L. S. Scaturro, and S. Wolfe, Phys. Rev. Lett. **43**, 274 (1979).
[33]A. Henglein, J. Phys. Chem. **76**, 3883 (1972).
[34]M. J. Brunger, S. J. Buckman, L. J. Allen, I. E. McCarthy, and K. Ratnavelu, J. Phys. B **25**, 1823 (1992).
[35]R. Carlson, in *Methods of Experimental Physics*, edited by G. Weissler and R. Carlson (Academic, New York, 1979), Vol. 14, Chap. 1.2.
[36]R. Schneider, D. Reiter, H. P. Zehrfeld, B. J. Braams, M. Baelmans, J. Geiger, H. Kastelewicz, J. Neuhauser, and R. Wunderlich, J. Nucl. Mater. **196 & 198**, 810 (1992).
[37]For example: S. A. Cohen, K. A. Werley, D. E. Post, B. J. Braams, J. L. Perkins, and D. Pearlstein, J. Nucl. Mater. **176 & 177**, 909 (1990); G. P. Maddison, E. S. Hotston, D. Reiter, P. Börner, and T. Baelmans, *Proceedings, 18th EPS Conference Controlled Fusion Plasma Physics*, Berlin (European Physical Society, Petit-Lancy, 1991), p. 197.
[38]S. Braginskii, in *Review of Plasma Physics*, edited by M. Leontovich (Consultant Bureau, New York, 1965), Vol. 1, p. 205.
[39]R. K. Porteous and D. B. Graves, IEEE Trans. Plasma Sci. **PS-19**, 204 (1991).
[40]R. Janev, W. Langer, K. Evans, Jr., and D. Post, Jr., *Elementary Processes in Hydrogen–Helium Plasmas* (Springer-Verlag, New York, 1987).
[41]F. Chen, *Introduction to Plasma Physics* (Plenum, New York, 1985).
[42]R. Bissell, P. Johnson, and P. Stangeby, Phys. Fluids B **1**, 1133 (1989).
[43]D. A. Knoll, P. R. McHugh, S. I. Krasheninnikov, and D. J. Sigmar, Phys. Plasmas **3**, 293 (1996).
[44]See for example, R. Schneider, D. Reiter, D. Coster, J. Neuhauser, K. Lackner, and B. Braams, J. Nucl. Mater. **220–222**, 1076 (1995); A. Taroni, G. Corrigan, R. Simonini, J. Spence, and S. Weber, *ibid*. 1086 (1995).